

# Constrained Form-Finding of Tension-Compression Structures using Automatic Differentiation

Rafael Pastrana<sup>a,\*</sup>, Patrick Ole Ohlbrock<sup>b</sup>, Thomas Oberbichler<sup>c</sup>, Pierluigi D’Acunto<sup>d</sup>, Stefana Parascho<sup>a</sup>

<sup>a</sup>CREATE Laboratory, School of Architecture, Princeton University, United States of America

<sup>b</sup>Chair of Structural Design, Institute of Technology in Architecture, ETH Zürich, Switzerland

<sup>c</sup>Chair of Structural Analysis, Technische Universität München, Germany

<sup>d</sup>Professorship of Structural Design, Technische Universität München, Germany

## Abstract

This paper proposes a computational approach to form-find pin-jointed, bar structures subjected to combinations of tension and compression forces. The generated equilibrium states can meet force and geometric constraints via gradient-based optimization. We achieve this by extending the Combinatorial Equilibrium Modeling (CEM) framework in three important ways. Firstly, we introduce a new topological object, the auxiliary trail, to expand the range of structures that can be form-found with the framework. Secondly, we leverage automatic differentiation (AD) to obtain an exact value of the gradient of the sequential and iterative calculations of the CEM form-finding algorithm, instead of a numerical approximation. We finally encapsulate our research developments into an open-source design tool written in Python that is usable across different CAD platforms and operating systems. After studying four different structures – a self-stressed planar tensegrity, a tree canopy, a curved suspension bridge, and a spiral staircase – we show that our approach allows solving constrained form-finding problems on a diverse range of structures more efficiently than in previous work.

**Keywords:** form-finding, optimization, automatic differentiation, design tool, structural design, combinatorial equilibrium modeling

## 1. Introduction

A *form-finding* method generates the shape and the internal force state of a structure so that, given a design load case and a set of support conditions, the structure is in a state of *static equilibrium* [1, 2]. Different numerical form-finding methods exist but they fall into one of three categories: stiffness-matrix [3, 4], dynamic equilibrium [5–7] and geometric [8–15] approaches. An in-depth review of this taxonomy is found in [1, 16]. Developments in all categories have been propelled over the last decade by the development of multiple computational design tools [17–21].

In these form-finding approaches, a structure is often modeled as a discrete network of straight bars that are connected by pinned joints at the nodes. The design load is transferred from node to node exclusively through axial forces in the bars and a state of static equilibrium is reached when the sum of forces incident to every node is zero. Conceptually, the axial-dominant load-carrying mechanism of a structure in static equilibrium implies that it will require less material volume to withstand the applied design load [22].

### 1.1. The CEM framework

The Combinatorial Equilibrium Modeling (CEM) framework is a geometric form-finding method for spatial structures mod-

eled as pin-jointed bar networks and subjected to combinations of tension and compression forces [23, 24]. Examples of such mixed systems are space frames, bridges, stadium roofs, multistory buildings and tensegrities.

The framework consists of two operative parts: the CEM form-finding algorithm and an optimization-based constrained form-finding solver. Moreover, this framework represents a structure with three diagrams: A topology diagram  $T$  describes its internal connectivity and internal tension-compression state. Meanwhile, a form diagram  $F$  and a force diagram  $F^*$  display the geometric and force attributes of the calculated state of static equilibrium. Figure 1 presents a graphical overview of how these components interact and Section 2 provides a thorough review of their underpinnings.

A distinctive feature of the CEM form-finding algorithm is that equilibrium is computed sequentially and iteratively, unlike other geometric form-finding methods [8–10, 25]. Nevertheless, this computation approach is precisely what allows the CEM form-finding algorithm to ensure the generation of a static equilibrium state for a mixed tension-compression structure as long as an input topology diagram  $T$  fulfills the requirements listed in Section 1.2.1.

The CEM algorithm allows designers to explore different equilibrium states for a fixed diagram  $T$  by manipulating a portion of the nodal positions, and a subset of the bar forces and lengths of a structure (see Section 2.2). However, realistic structural design scenarios often pose geometrical and force

\*Corresponding author

Email address: arpj@princeton.edu (Rafael Pastrana)

constraints a priori where it is more relevant to find a specific equilibrium state that best satisfies them. Examples of such constraints include fitting a target shape [26, 27], restraining bar forces and lengths [28–30], and controlling the reaction forces at the supports of a structure [20, 31, 32]. The challenge is that while the design constraints can be readily enumerated, it is often not straightforward to discern what combination of input design parameters is conducive to the envisioned result.

One way to solve such a constrained form-finding problem is to manually tweak the input design parameters until the required constraints are met, one by one. This can quickly become a cumbersome process. Instead, the CEM framework form-finds spatial structures subjected to geometrical and force constraints following an automatic approach: constraints are aggregated into a single objective function and a computer assists the designer in calculating the values of the design parameters that minimize it via gradient-based optimization [24, 33].

### 1.2. Limitations of the CEM framework

The CEM framework as presented in [23, 24, 33] faces two limitations. One of them is related to its topological modeling flexibility and the other to its computational performance when solving a constrained form-finding problem.

#### 1.2.1. Strict topological modeling rules

Every topology diagram  $T$  must fulfill two requirements in order to be considered a valid input to the CEM form-finding algorithm:

1. Every node  $\mathbf{v}$  needs to be part of only one trail  $\omega$  (see Section 2.1.1).
2. Every trail  $\omega$  must have only one support assigned to its last node.

Abiding by these two rules restricts the type of structures that the CEM algorithm can form-find. Adequately constructing a valid topological diagram can become a daunting task without a sound knowledge of the CEM theoretical background, especially for structures that do not have a clear load-transfer hierarchy.

Figure 2a shows the topological diagram of a structure in which the two topological rules are satisfied. In contrast, the diagram in Figure 2b violates the first rule because the two proposed trails  $\omega_1 = \{1, 3, 4\}$  and  $\omega_2 = \{2, 3, 4\}$  share nodes 3 and 4. Figure 2c depicts a planar, self-stressed tensegrity structure which by definition has no supports and consequently infringes rule number two.

#### 1.2.2. Approximate gradient computation

To solve a constrained form-finding problem, the CEM framework has approximated the gradient of the objective function to minimize via finite differences (FD) [24, 33]. This is in stark contrast to other geometric form-finding precedents where the analytical equations to calculate an exact gradient have been published [9, 26, 27, 32, 34, 35]. FD circumvents

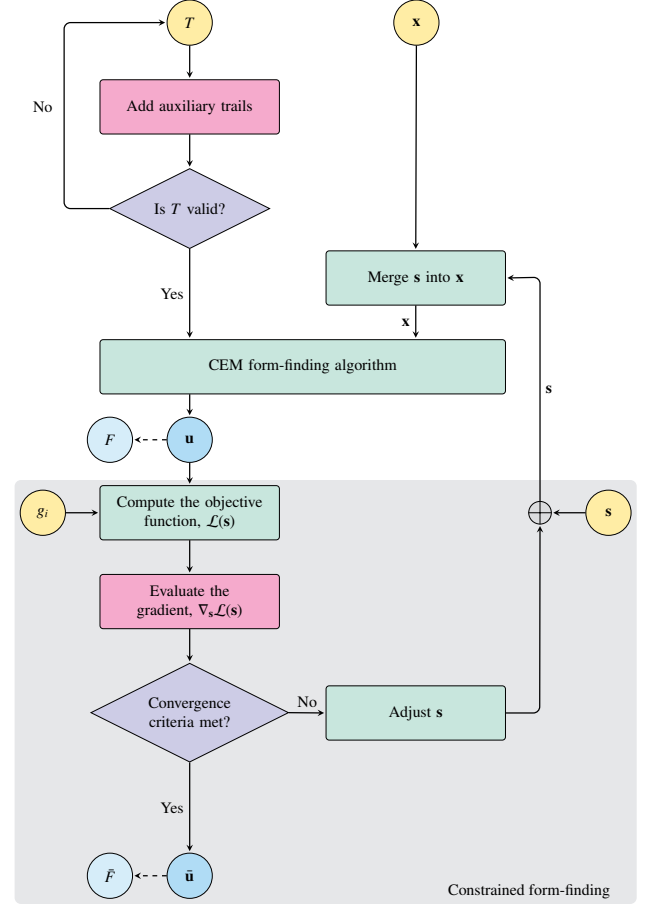


Figure 1: Overview of the Combinatorial Equilibrium Modeling (CEM) framework and our extensions. The inputs to the framework are a topology diagram  $T$  and the design parameters  $\mathbf{x}$ . The CEM form-finding algorithm calculates a state of static equilibrium  $\mathbf{u}$  from which a form diagram  $F$  can be optionally constructed. To find a constrained equilibrium state  $\bar{\mathbf{u}}$  that best satisfies force and geometric constraints  $g_i$ , the CEM framework minimizes an objective function  $\mathcal{L}(\mathbf{s})$  by iteratively adjusting the optimization parameters  $\mathbf{s}$  using the gradient  $\nabla_{\mathbf{s}}\mathcal{L}(\mathbf{s})$  until the convergence criteria  $\mathcal{L}(\mathbf{s}) < \epsilon$  or  $\|\nabla_{\mathbf{s}}\mathcal{L}(\mathbf{s})\| < \epsilon$  is reached. Two of the extensions we make in this paper are highlighted in pink. Auxiliary trails simplify the construction of a larger variety of valid topology diagrams  $T$ . Reverse-mode automatic differentiation computes an exact value of  $\nabla_{\mathbf{s}}\mathcal{L}(\mathbf{s})$  thus allowing for more efficient and stable solutions to constrained form-finding problems.

the derivation problems we discuss in Section 3.2 as it does not require the calculation of analytical derivatives of the CEM form-finding algorithm to obtain a gradient estimate.

Using FD poses a number of challenges nonetheless. FD requires choosing an adequate step size  $h$  to compute the gradient approximation [36]. If the resulting step size  $h$  is too large, the gradient approximation can be inaccurate, whereas if it is too small it can lead to significant round-off errors due to numerical underflow. Moreover, calculating gradients with FD is computationally taxing as the objective function has to be evaluated at least once per every optimization parameter input [36, 37]. This can be detrimental to an interactive exploration of static equilibrium states for a structure, particularly if the number of optimization parameters is large.

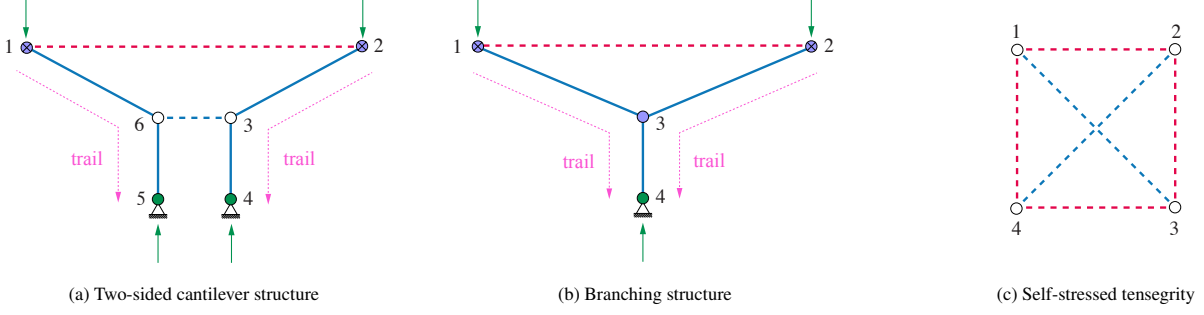


Figure 2: Topology diagrams  $T$  that correspond to three different structural systems. Note that diagrams 2b and 2c do not meet the CEM topology requirements listed in Section 1.2. The former shows nodes 3 and 4 as members of two different trails,  $\omega_1$  and  $\omega_2$ , whereas the latter defines neither trails nor support nodes.

### 1.3. Automatic differentiation

*Automatic differentiation* (AD), also known as algorithmic differentiation, comprises a set of techniques that evaluate the derivative of a differentiable function that is expressed algorithmically [38]. In contrast to FD, derivatives obtained with AD are exact up to computer precision and do not require the specification of a step size  $h$  to be computed [36]. Unlike symbolic differentiation, derivatives can be evaluated with AD through control flow statements, such as if-else clauses, loops and recursion [38].

One of the prominent applications of AD today is in training machine learning models via backpropagation, in particular neural architectures that learn via gradient-based optimization [39]. Other precedents of AD applied to various engineering problems are the sizing of the frame of an injection molding machine [37], the shape optimization of a supersonic aircraft [40], and the weight minimization of steel frames under seismic loads [41]. In addition to its ease of use, AD is also characterized by its high performance. For example, AD has been used to automatically derive complex isogeometric elements from an energy functional [42].

In the context of form-finding, Cuvilliers recently proposed to use AD in form-finding framework for structures subjected to geometric constraints [43]. Unlike their work, we use the CEM form-finding algorithm and not the *Force Density Method* (FDM) [8, 9] as the equilibrium state calculator. Furthermore, they focus on compression-only shells while we study various types of mixed tension-compression structures.

### 1.4. Outline and contribution

This paper is organized in six sections. In Section 2 we present the theoretical concepts that underpin the current state

of the CEM framework. The steps followed to sequentially and iteratively compute a state of static equilibrium are reviewed from an algorithmic perspective. The mathematical formulation of the objective function that is minimized to solve a constrained form-finding problem is also discussed.

Section 3 develops the extensions we make to the CEM framework to overcome the limitations we outlined in Section 1.2, which constitute the core of our contribution. We first introduce a new topological helper object, the auxiliary trail. We show next how we leverage AD to evaluate an exact gradient of the CEM form-finding algorithm and guide the reader through this process with a simple constrained form-finding example. We also present a new standalone design tool called `compas_cem` that encapsulates the two above-mentioned extensions.

In Section 4, we benchmark and validate the extended CEM framework by studying multiple constrained form-finding problems on three different types of structures: a self-stressed tensegrity, a tree canopy and a curved suspension bridge subjected to torsional loads. The applicability of our work in practical structural design problems is showcased in the case study of a spiral staircase in Section 5.

The paper concludes in Section 6 with a discussion of our experimental findings, the limitations of our approach, its potential relation to other geometric form-finding methods, and future research directions.

## 2. Theoretical background

We review how the Combinatorial Equilibrium Modeling (CEM) framework works. This is relevant to guide the discussion in subsequent sections. The CEM framework was introduced in [23] and further developed in [24, 33]. It consists of two operative parts: (i) a form-finding algorithm that builds equilibrium sequentially and iteratively (Section 2.3), and (ii) a constrained form-finding routine that utilizes an optimization solver (Section 2.4). The goal of the former is to generate a numerical *state of static equilibrium*,  $\mathbf{u}$ . That of the latter is to produce a *constrained state of static equilibrium*  $\bar{\mathbf{u}}$  that has been restricted by a set of geometric and force constraints. Regardless, there are two necessary inputs to calculate these states: a valid topology diagram  $T$  and a vector of design parameters  $\mathbf{x}$ .

Symbol	Description	Symbol	Description
○	Node	—	Trail edge
⊗	Node with load	-----	Deviation edge
●	Origin node	—	Edge in tension
●	Support node	—	Edge in compression
→	Force vector	—	Auxiliary trail

Table 1: Symbols used to represent topology  $T$  and form diagrams,  $F$ .

### 2.1. Topology diagram

A *topology diagram*  $T$  is an undirected graph of  $N$  nodes  $\mathcal{V}$  connected by  $M$  edges  $\mathcal{E}$ . It captures the internal connectivity of a structure modeled as a pin-jointed network of straight bars. Every edge  $\mathbf{e}_{i,j}$  connecting two nodes  $\mathbf{v}_i, \mathbf{v}_j$  must be labeled as either a *trail edge*  $\mathbf{e}_{i,j}^t$  or a *deviation edge*,  $\mathbf{e}_{i,j}^d$ . Trail edges encode the primary load paths of a structure, while deviation edges are used to sculpt these load paths in their way towards the supports of a structure [23]. The entries in the adjacency matrix  $\mathbf{C} \in \{-1, 0, 1\}$  of the topology diagram define the expected internal force state  $c_{i,j}$  of the bars in the structure [24]. If  $\mathbf{C}[i, j] = c_{i,j} = -1$ , the corresponding edge  $\mathbf{e}_{i,j}$  is in compression. Conversely, if  $c_{i,j} = 1$ , then  $\mathbf{e}_{i,j}$  is in tension. A topology diagram furthermore prescribes the subset of size  $L$  with the nodes  $\mathcal{S}$  where a support is assigned,  $\mathcal{S} \subset \mathcal{V}$ .

#### 2.1.1. Trails

Trails are critical to evaluate the validity of a topology diagram  $T$ , as discussed in Section 1.2.1. A *trail*  $\omega$  is an ordered set of nodes that are linked exclusively by trail edges,  $\omega = \{\mathbf{v}^0, \dots, \mathbf{v}^s\}$ . The first node in a trail  $\mathbf{v}^0$  is referred to as an *origin node*. The last node  $\mathbf{v}^s$  must have a support assigned,  $\mathbf{v}^s \in \mathcal{S}$ , and it is thus referred to as a *support node*. A trail must contain at least two nodes. The set of all trails in a topology diagram is denoted  $\Omega$ . In principle, there must be as many trails as there are support nodes,  $|\mathcal{S}| = |\Omega|$ . Trails need not be all equal-sized.

#### 2.1.2. Sequences

Once a trail  $\omega$  is constructed, the nodes within are sorted based on how distant they are to the origin node  $\mathbf{v}^0$  in the trail. For every node  $\mathbf{v}$ , this topological distance is defined as the number of intermediate trail edges  $\mathbf{e}^t$  plus one between  $\mathbf{v}$  and  $\mathbf{v}^0$ . Nodes that are equally distant to their corresponding  $\mathbf{v}^0$  belong to the same *sequence*,  $k$ . While the first sequence  $k = 1$  groups all the origin nodes  $\mathbf{v}^0$  in all possible trails  $\Omega$ , the last sequence  $k_{\max}$  contains the support nodes of the longest trails (i.e. the trails with the greater number of nodes).

### 2.2. Design parameters

The vector of design parameters  $\mathbf{x}$  prescribes an immutable portion of the state of static equilibrium  $\mathbf{u}$  that is calculated by the CEM form-finding algorithm. It concatenates:

- A vector  $\boldsymbol{\mu} \in \mathbb{R}_+^M$  with the absolute magnitude of the internal force  $\mu_{i,j}^d$  of every deviation edge  $\mathbf{e}_{i,j}^d$ .
- A vector  $\boldsymbol{\lambda} \in \mathbb{R}_+^M$  with the length  $\lambda_{i,j}^t$  of each trail edge  $\mathbf{e}_{i,j}^t$ .
- A matrix  $\mathbf{P} \in \mathbb{R}^{N \times 3}$  with the position  $\mathbf{p}^0$  of every origin node  $\mathbf{v}^0$
- A matrix  $\mathbf{Q} \in \mathbb{R}^{N \times 3}$  with the load vectors  $\mathbf{q}$  applied to the nodes  $\mathbf{v}$ . Only one load vector per node is permitted. If the modeled structure is self-stressed, all the entries in  $\mathbf{Q}$  are null vectors.

### Algorithm 1: The CEM form-finding algorithm

---

**Input** : Topology diagram,  $T$   
Design parameters,  $\mathbf{x}$   
Maximum # of equilibrium iterations,  $t_{\max}$   
Minimum distance threshold,  $\eta_{\min}$

**Output**: State of static equilibrium,  $\mathbf{u}$

```

1  $\mathcal{V}, \mathcal{E}, \mathcal{S}, \Omega, \mathbf{C} \leftarrow T$ ;
2  $\boldsymbol{\mu}, \boldsymbol{\lambda}, \mathbf{P}, \mathbf{Q} \leftarrow \mathbf{x}$ ;
3  $\mathbf{T}, \mathbf{R} \leftarrow [\text{empty}]$ ;
4  $t \leftarrow 1$ ;
5  $\eta \leftarrow \infty$ ;
6 while  $t \leq t_{\max}$  or  $\eta \geq \eta_{\min}$  do
7    $k \leftarrow 1$ ;
8    $\mathbf{P}^{(t-1)} \leftarrow \mathbf{P}$ ;
9   while  $k \leq k_{\max}$  do
10    for  $\omega \in \Omega$  do
11      if  $k \leq |\omega|$  then
12         $i \leftarrow \omega[k]$ ;
13         $\mathbf{t}_h \leftarrow \mathbf{0}$ ;
14        if  $k > 1$  then
15           $h \leftarrow \omega[k-1]$ ;
16           $\mathbf{t}_h \leftarrow \mathbf{T}[h]$ ;
17         $\mathbf{d}_i \leftarrow \text{deviation\_v}(i, t, \mathbf{P}, T)$ ;  $\triangleright$  Eq. 3
18         $\mathbf{q}_i \leftarrow \mathbf{Q}[i]$ ;
19         $\mathbf{t}_i \leftarrow \mathbf{t}_h - \mathbf{d}_i - \mathbf{q}_i$ ;  $\triangleright$  Eq. 2
20        if  $i \notin \mathcal{S}$  then
21           $j \leftarrow \omega[k+1]$ ;
22           $\lambda_{i,j}^t \leftarrow \lambda[i, j]$ ;
23           $c_{i,j} \leftarrow \mathbf{C}[i, j]$ ;
24           $\mu_{i,j}^t \leftarrow \|\mathbf{t}_i\|$ ;  $\triangleright$  Eq. 4
25           $\mu[i, j] \leftarrow \mu_{i,j}^t$ ;
26           $\mathbf{p}_i \leftarrow \mathbf{P}[i]$ ;
27           $\mathbf{p}_j \leftarrow \mathbf{p}_i + c_{i,j} \lambda_{i,j}^t \frac{\mathbf{t}_i}{\|\mathbf{t}_i\|}$ ;  $\triangleright$  Eq. 1
28           $\mathbf{P}[j] \leftarrow \mathbf{p}_j$ ;
29           $\mathbf{T}[i] \leftarrow \mathbf{t}_i$ ;
30        else
31           $\mathbf{R}[i] \leftarrow \mathbf{t}_i$ ;
32          break
33       $k \leftarrow k + 1$ ;
34    for  $\mathbf{e}_{i,j}^d \in \mathcal{E}$  do
35       $i, j \leftarrow \mathbf{e}_{i,j}^d$ ;
36       $\lambda_{i,j}^d \leftarrow \|\mathbf{P}[i] - \mathbf{P}[j]\|$ ;  $\triangleright$  Eq. 5
37       $\lambda[i, j] \leftarrow \lambda_{i,j}^d$ ;
38     $\eta \leftarrow 0$ ;
39    for  $i \in \mathcal{V}$  do
40       $\eta \leftarrow \eta + \|\mathbf{P}[i] - \mathbf{P}^{(t-1)}[i]\|$ ;  $\triangleright$  Eq. 6
41     $t \leftarrow t + 1$ ;
42  $\mathbf{u} \leftarrow \boldsymbol{\mu}, \boldsymbol{\lambda}, \mathbf{P}, \mathbf{Q}, \mathbf{R}$ ;

```

---

### 2.3. Form-finding algorithm

The CEM form-finding algorithm completes the attributes in  $\mathbf{u}$ . The logic of how the algorithm accomplishes this is provided in Algorithm 1. Concretely, its numerical outputs are:

- The absolute magnitude of the internal force  $\mu_{i,j}^t \in \mu$  of every trail edge  $\mathbf{e}_{i,j}^t$ .
- The length  $\lambda_{i,j}^d \in \lambda$  of every deviation edge  $\mathbf{e}_{i,j}^d$ .
- The position  $\mathbf{p}_i \in \mathbf{P}$  of every non-origin node,  $\mathbf{v}_i \neq \mathbf{v}_i^o$ .
- A matrix  $\mathbf{R} \in \mathbb{R}^{L \times 3}$  with the reaction force vector  $\mathbf{r}_i$  incident to every support node,  $\mathbf{v}_i^s \in \mathbf{S}$ .

These are concatenated into a single vector. Once  $\mathbf{u}$  is complete, the form diagram  $F$  and the force diagram  $F^*$  of the structure can be built using vector-based graphic statics [14] to visualize the resulting equilibrium state of the structure.

### 2.3.1. Sequential equilibrium

Static equilibrium is calculated at the nodes of the diagram  $T$  one sequence at a time [23, 24]. The form-finding process starts off by computing equilibrium at the nodes at the first sequence,  $k = 1$  and continues to the next sequence  $k + 1$  until the farthest one,  $k_{\max}$ , is reached. The calculation ends for every trail  $\omega$  when the node at the current sequence  $k$  is a support node.

Except for the nodes at the first sequence  $k = 1$ , a state of static equilibrium at node  $\mathbf{v}_j$  at sequence  $k \neq 1$  is subordinated to the equilibrium state of the nodes preceding it. Let the triplet of nodes  $\mathbf{v}_h$ ,  $\mathbf{v}_i$  and  $\mathbf{v}_j$  be three consecutive nodes along a sequence-ordered trail  $\omega$ . Let  $\mathbf{v}_i$  be the node on the trail at sequence  $k$ ,  $\mathbf{v}_h$  the node at the previous sequence  $k - 1$  and  $\mathbf{v}_j$  the node at the next sequence  $k + 1$ . Calculating static equilibrium at node  $\mathbf{v}_i$  begets the position  $\mathbf{p}_j$  of the next node  $\mathbf{v}_j$  and the force magnitude  $\mu_{i,j}^t$  of the trail edge  $\mathbf{e}_{i,j}^t$  connecting them. The position  $\mathbf{p}_j$  is described as

$$\mathbf{p}_j = \mathbf{p}_i + c_{i,j} \lambda_{i,j}^t \frac{\mathbf{t}_i}{\|\mathbf{t}_i\|} \quad (1)$$

where  $\mathbf{p}_i$  is the position of node  $\mathbf{v}_i$ ,  $c_{i,j}$  and  $\lambda_{i,j}^t$  are the internal force state ( $-1$  for compression,  $1$  for tension) and the length of  $\mathbf{e}_{i,j}^t$ , respectively. The vector  $\mathbf{t}_i$  is the residual force incident to the node  $\mathbf{v}_i$ . To estimate it, all the forces acting on  $\mathbf{v}_i$  are summed:

$$\mathbf{t}_i = \mathbf{t}_h - \mathbf{d}_i - \mathbf{q}_i \quad \text{where} \quad \mathbf{t}_h = \begin{cases} \mathbf{0} & \text{if } k = 1 \\ \mathbf{t}_h & \text{otherwise} \end{cases} \quad (2)$$

The vector  $\mathbf{q}_i$  denotes the load applied to node  $\mathbf{v}_i$ , if any, and  $\mathbf{d}_i$  corresponds to the sum of all the force vectors stemming from the set of deviation edges  $\mathcal{M}_i$  connected to  $\mathbf{v}_i$ :

$$\mathbf{d}_i = \sum_m^{M_i} c_{i,m} \mu_{i,m}^d \frac{\mathbf{p}_i - \mathbf{p}_m}{\|\mathbf{p}_i - \mathbf{p}_m\|} \quad (3)$$

The terms  $c_{i,m}$ ,  $\mu_{i,m}^d$  and  $\mathbf{p}_m$  encode the force state, force magnitude and the position of the node  $\mathbf{v}_m$  that is connected to  $\mathbf{v}_i$  by the deviation edge  $\mathbf{e}_{i,m}^d$ . If no deviation edges are connected to  $\mathbf{v}_i$ , then  $\mathbf{d}_i = \mathbf{0}$ .

To maintain the equilibrium of forces at  $\mathbf{v}_i$ , the residual vector  $\mathbf{t}_i$  is taken by the trail edge  $\mathbf{e}_{i,j}^t$  such that the vector formed between positions  $\mathbf{p}_i$  and  $\mathbf{p}_j$  point in the same direction as  $\mathbf{t}_i$ ,

Type	Target	Constraint function
Geometry	Node position, $\bar{\mathbf{p}}_i$	$g_1(\mathbf{u}(\mathbf{s})) = \ \mathbf{p}_i - \bar{\mathbf{p}}_i\ $
	Edge orientation, $\bar{\mathbf{a}}_{i,j}$	$g_2(\mathbf{u}(\mathbf{s})) = \left  \frac{\mathbf{p}_j - \mathbf{p}_i}{\ \mathbf{p}_j - \mathbf{p}_i\ } \cdot \bar{\mathbf{a}}_{i,j} \right  - 1$
	Edge length, $\bar{\lambda}_{i,j}^d$	$g_3(\mathbf{u}(\mathbf{s})) = \lambda_{i,j}^d - \bar{\lambda}_{i,j}^d$
Force	Edge force, $\bar{\mu}_{i,j}^t$	$g_4(\mathbf{u}(\mathbf{s})) = \mu_{i,j}^t - \bar{\mu}_{i,j}^t$
	Edge load path, $\bar{\varphi}_{i,j}$	$g_5(\mathbf{u}(\mathbf{s})) = \mu_{i,j} \lambda_{i,j} - \bar{\varphi}_{i,j}$
	Reaction force, $\bar{\mathbf{r}}_i$	$g_6(\mathbf{u}(\mathbf{s})) = \ \mathbf{r}_i - \bar{\mathbf{r}}_i\ $

Table 2: Constraint functions supported by the CEM framework. From a geometrical vantage point,  $g_1$  sets a target position  $\bar{\mathbf{p}}_i$  for node  $\mathbf{v}_i$ ;  $g_2$  a target orientation vector  $\bar{\mathbf{a}}_{i,j}$  for edge  $\mathbf{e}_{i,j}$ ; while  $g_3$  a target length  $\bar{\lambda}_{i,j}^d$  for deviation vector  $\mathbf{e}_{i,j}^d$ . Similarly, but from a force perspective,  $g_4$  prescribes a desired force magnitude  $\bar{\mu}_{i,j}^t$  for trail edge  $\mathbf{e}_{i,j}^t$ ;  $g_5$  a target load path  $\bar{\varphi}_{i,j}$  for edge  $\mathbf{e}_{i,j}$ ; and  $g_6$  a target reaction force vector  $\bar{\mathbf{r}}_i$  at support node  $\mathbf{v}_i^s$ .

and the absolute magnitude of the force passing through the edge  $\mu_{i,j}^t$  is equal to the norm of  $\mathbf{t}_i$ :

$$\mu_{i,j}^t = \|\mathbf{t}_i\| \quad (4)$$

If  $\mathbf{v}_j$  is a support node the residual vector  $\mathbf{t}_i$  is parsed as the reaction force vector incident to the support node  $\mathbf{v}_i^s$ ,  $\mathbf{r}_i = \mathbf{t}_i$ . The length of any deviation edge  $\mathbf{e}_{i,j}^d$  is lastly calculated as the norm of the distance vector between the positions of the two nodes it links:

$$\lambda_{i,j}^d = \|\mathbf{p}_j - \mathbf{p}_i\| \quad (5)$$

### 2.3.2. Iterative equilibrium

The process described in Section 2.3.1 must be run iteratively whenever (i) form-dependent load cases like wind or self-weight are applied; or (ii) deviation edges  $\mathbf{e}_{i,j}^d$  that connect any two nodes  $\mathbf{v}_i$ ,  $\mathbf{v}_j$  that do not belong to the same sequence  $k$  exist (also called *indirect deviation edges*) [24]. The termination conditions here are to exhaust a maximum number of iterations  $t_{\max}$  or to reach a minimum distance threshold  $\eta_{\min}$  close to zero, such that  $\eta \leq \eta_{\min}$ :

$$\eta = \sum_i^{\mathcal{V}} \|\mathbf{p}_i^{(t)} - \mathbf{p}_i^{(t-1)}\| \quad (6)$$

The distance  $\eta$  measures the cumulative displacement of the position  $\mathbf{p}_i$  of every node  $\mathbf{v}_i$  at iteration  $t$  in relation to the previous one. The value of  $\eta$  can be normalized by dividing it by  $N$  to make it independent of the total number of nodes in the structure. If indirect deviation edges exist, their contribution to  $\mathbf{d}_i$  in Equation 3 is set to  $\mathbf{0}$  during the first iteration,  $t = 1$  [24].

### 2.4. Constrained form-finding

The CEM framework can determine the parameters that lead to a constrained state of static equilibrium  $\bar{\mathbf{u}}$  that best satisfies a priori geometric and structural design requirements. This is accomplished by minimizing an objective function using gradient-based optimization.



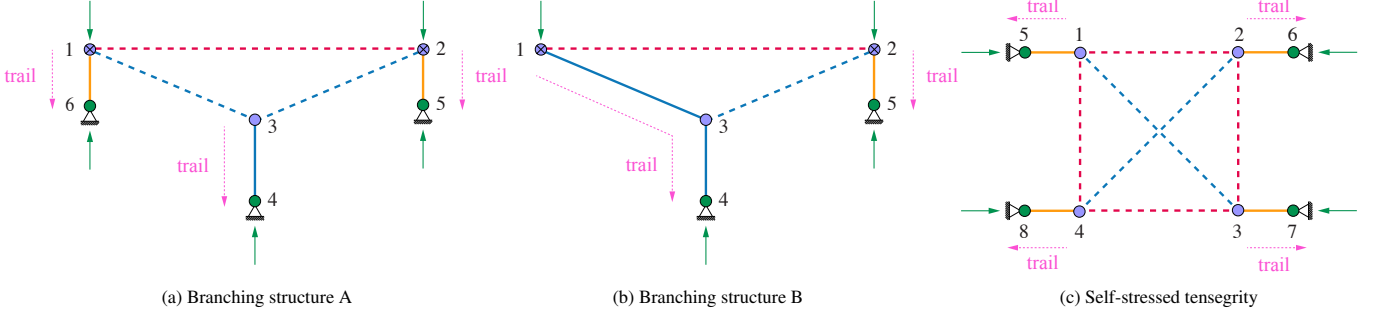


Figure 3: Auxiliary Trails. To ensure topological validity, one (3b) and two (3a) auxiliary trails are appended to the topology diagram  $T$  of the branching structure first displayed in Figure 2b. Similarly, four auxiliary trails are inserted to the topology diagram of the self-stressed structure in Figure 3c

#### 2.4.1. Optimization parameters

The vector of optimization parameters  $\mathbf{s}$  defines the potential solution space of a constrained form-finding problem. It collects a subset of the design parameters  $\mathbf{x}$  (see Section 2.2). Design parameters that are not included in  $\mathbf{s}$  stay constant throughout the optimization process.

#### 2.4.2. System solution

The CEM form-finding algorithm provides an explicit solution  $\mathbf{u}(\mathbf{s})$  for a given a choice of optimization parameters  $\mathbf{s}$ . As per Section 2.3, this solution contains the missing node positions  $\mathbf{p}$ , the internal forces in the trail edges  $\mu^t$ , the lengths of the deviation edges  $\lambda^d$ , and the reaction forces at the supports  $\mathbf{r}$ . The output solution described by  $\mathbf{s}$  and  $\mathbf{u}(\mathbf{s})$  is in static equilibrium.

#### 2.4.3. Constraints

Vector  $\mathbf{s}$  is modified to satisfy nonlinear equality constraints. Each constraint  $g_i$  is formulated as a function of the optimization parameters and the system solution  $\mathbf{u}(\mathbf{s})$ :

$$g_i(\mathbf{u}(\mathbf{s})) = 0 \quad (7)$$

The constraint functions  $g_i$  can be formulated arbitrarily. However, the complexity of the formulation may affect the solution and the convergence rate of the problem. We list in Table 2 the most frequently used geometric- and force-related constraint functions which measure the distance between the current value and a target value for one of the attributes in  $\mathbf{u}(\mathbf{s})$ . These functions can be freely combined in Equation 8.

#### 2.4.4. Objective function

Every nonlinear equality constraint  $g_i$  is weighted by a penalty factor  $w_i$  and aggregated in a single objective function  $\mathcal{L}$  that is minimized to solve a constrained form-finding problem.

$$\mathcal{L}(\mathbf{s}) = \frac{1}{2} \sum_i w_i g_i(\mathbf{u}(\mathbf{s}))^2 \quad (8)$$

#### 2.4.5. Gradient-based optimization

Equation 8 can be efficiently minimized using first-order gradient descent or any other gradient-based optimization algorithm, such as the Limited-Memory Broyden–Fletcher–Goldfarb–Shanno algorithm (L-BFGS) [44], Sequential Least Squares Programming (SLSQP) [45] or Truncated Newton (TNEWTON) [46].

An optimal instance of  $\mathbf{s}$  is produced when each of the defined constraints  $g_i(\mathbf{u}(\mathbf{s}))$  satisfies Equation 7 and thus the output value of the objective function is zero. Numerically,  $\mathbf{s}$  is deemed optimal when the  $\mathcal{L}(\mathbf{s})$  is smaller than a small numerical convergence threshold  $\epsilon$ . Such a solution is non-existent when the constraints contradict each other. Then, the optimizer halts when it finds a minimum of the objective function where the norm of the gradient vanishes,  $\|\nabla_{\mathbf{s}} \mathcal{L}(\mathbf{s})\| < \epsilon$ . The computation of the gradient is discussed in Section 3.2.

### 3. Extensions to the CEM framework

We extend the CEM framework to overcome the limitations outlined in Section 1.2: auxiliary trails facilitate the creation of a valid topology diagram  $T$  and automatic differentiation enables the computation of more reliable and efficient solutions to constrained form-finding problems. The extended CEM framework is implemented in a standalone design tool.

#### 3.1. Auxiliary trails

An auxiliary trail  $\omega^a = \{\mathbf{v}_i^o, \mathbf{v}_j^s\}$  is a short helper trail with an origin node  $\mathbf{v}_i^o$  and a support node  $\mathbf{v}_j^s$  linked by a single trail edge  $\mathbf{e}_{i,j}^t$  of unit length  $\lambda_{i,j}^t = 1$ . We automatically attach an auxiliary trail to any node  $\mathbf{v}_i$  in a topology diagram  $T$  that has not been assigned to another trail before the application of the CEM form-finding algorithm (see Section 2.3). Such trail-free nodes are characteristic at the intersection between one or more deviation edges and no trail edges. The attachment operation transforms node  $\mathbf{v}_i$  into the origin node  $\mathbf{v}_i^o$  of  $\omega^a$ .

The extensive use of auxiliary trails enables the explicit construction of the topology diagram  $T$  of a structure using only deviation edges. Given an input  $T$  wherein every bar of a structure is modeled as a deviation edge  $\mathbf{e}_{i,j}^d$ , appending an auxiliary trail to every node  $\mathbf{v}_i$  in  $T$  converts this initially invalid diagram into a diagram  $T$  that complies with the topological

modeling rules of the CEM form-finding algorithm (Section 1.2.1). Such a deviation-only modeling strategy circumvents the manual edge labeling process described in Section 2.1 as no distinction has to be made upfront by a designer on whether an edge  $\mathbf{e}_{i,j}$  is a trail edge  $\mathbf{e}_{i,j}^t$  or a deviation edge  $\mathbf{e}_{i,j}^d$ . We show two examples of structures that are modeled using the deviation-only modeling strategy in Sections 4.1 and 4.2.

However, the topological modeling flexibility enabled by auxiliary trails comes at a computation price. The attachment of an auxiliary trail creates a local artificial subsystem wherein a specific state of static equilibrium must be computed: the auxiliary trails must not carry any loads in order to capture the originally intended load-carrying behavior of the structure. An analogy for the role auxiliary trails play is that they provide additional temporary support to a structure while it is being form-found. Since we are interested in the "self-standing" version of the structure, an equilibrium state must be found in which the loads these temporary supports carry are zeroed out.

Form-finding a structure whose topology diagram  $T$  contains at least one auxiliary trail hence becomes a constrained form-finding task. The initially-desired static equilibrium state for a structure is obtained only after solving the optimization problem discussed in Section 2.4, where the objective function  $\mathcal{L}$  is extended with extra penalty terms we show in Equation 9.

$$\frac{1}{2} \sum_a w_a (\mu_{i,j}^t - \bar{\mu}_{i,j}^t)_a^2 \quad (9)$$

The purpose of the additional penalty terms is to minimize the difference between the target force  $\bar{\mu}_{i,j}^t$  and the actual force  $\mu_{i,j}^t$  in the trail edge  $\mathbf{e}_{i,j}^t$  of each auxiliary trail  $\omega^a$  in  $T$ . These terms are equivalent to constraint function  $g_4$  in Table 2. By extension, when the force in the trail edge of an auxiliary trail is zero  $\mu_{i,j}^t = 0$ , the reaction forces incident to its corresponding support node also vanish,  $\mathbf{r} = \mathbf{0}$ .

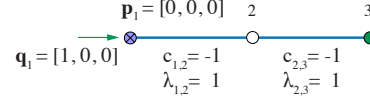
Figure 3 shows three topology diagrams  $T$  that use auxiliary trails to remedy the modeling challenges posed by the diagrams in Figure 2. Figure 3a depicts a diagram  $T$  where auxiliary trails  $\omega_2^a = \{1, 6\}$  and  $\omega_3^a = \{2, 5\}$  are appended to nodes 1 and 2. Meanwhile, in Figure 3b, trail  $\omega_2 = \{2, 3, 4\}$  is deleted, thus leaving node  $\mathbf{v}_2$  trail unassigned. An auxiliary trail  $\omega_2^a = \{2, 5\}$  is attached to  $\mathbf{v}_2$  to make  $T$  valid again. As portrayed by Figure 3c, an auxiliary trail is annexed to each of the four nodes of the tensegrity structure in Figure 2c to correct its initial topological invalidity.

### 3.2. Automatic and exact computation of the gradient

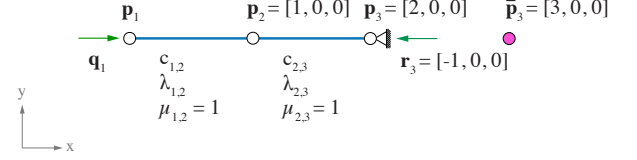
The gradient required to determine a minimum of Equation 8 results from the first derivative of  $\mathcal{L}$  with respect to the optimization parameters:

$$\nabla_s \mathcal{L} = \sum_i w_i g_i \cdot \nabla_s g_i \quad (10)$$

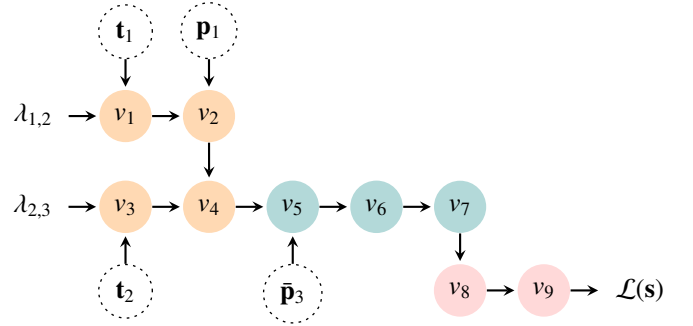
The computation of  $\nabla_s \mathcal{L}$  requires calculating the derivatives of the individual constraint functions  $\nabla_s g_i$  and the derivative of the system solution  $\mathbf{u}(\mathbf{s})$ :



(a) Topology diagram  $T$ , edge internal force states  $c_{1,2}, c_{2,3}$ ; and input design parameters  $\mathbf{x}$  (the position  $\mathbf{p}_1$  of origin node  $\mathbf{v}_1^0$ ; the edge lengths  $\lambda_{1,2}, \lambda_{2,3}$ ; and the applied node load  $\mathbf{q}_1$ ).



(b) Form diagram  $F$  and the equilibrium state  $\mathbf{u}$  generated with the CEM form-finding algorithm, which consists of the node positions  $\mathbf{p}_2, \mathbf{p}_3$ ; the edge absolute internal forces  $\mu_{1,2}, \mu_{2,3}$ ; and the support reaction force  $\mathbf{r}_3$ . To solve the constrained form-finding problem, position  $\mathbf{p}_3$  should reach the target position  $\bar{\mathbf{p}}_3$ .



(c) Computation graph that evaluates the objective function  $\mathcal{L}(\mathbf{s})$  at optimization parameters  $\mathbf{s} = [\lambda_{1,2}, \lambda_{2,3}]$ . This graph is built as part of the evaluation trace of reverse-mode AD. The nodes  $v_i$  store the output of all the intermediary operations that modify  $\mathbf{s}$  on their way to  $\mathcal{L}(\mathbf{s})$ . Nodes  $v_1$  to  $v_4$  correspond to operations that occur within the CEM form-finding algorithm (See Algorithm 1), while nodes  $v_5$  to  $v_7$  to those executed in the evaluation of the constraint function  $g_1$ . Nodes  $v_8$  and  $v_9$  evaluate Equation 8. Nodes with a dashed perimeter denote the constants that interact with  $\mathbf{s}$ . We unpack these operations in Table 3.

Figure 4: Constrained form-finding of a two-segment compression chain.

$$\nabla_s g_i = \frac{\partial g_i}{\partial \mathbf{u}} \frac{\partial \mathbf{u}}{\partial \mathbf{s}} \quad (11)$$

While Equations 1-6 are compact algebraic manipulations for which derivatives can be found analytically, manually applying the chain rule through the control flow structure of the CEM form-finding algorithm (see Algorithm 1) to calculate the partial derivative of the system solution with respect to the optimization parameters has been a complex task [24]. Instead of circumventing its sequential and iterative characteristics, we exploit the implementation of the CEM form-finding algorithm we develop in Section 3.3 by using AD in reverse mode to obtain a version of  $\nabla_s \mathcal{L}(\mathbf{s})$  that is exact up to floating-point precision. AD ingests the function  $\mathcal{L}$ , and generates another function that calculates the associated gradient  $\nabla_s \mathcal{L}(\mathbf{s})$ . The key insight is that  $\nabla_s \mathcal{L}(\mathbf{s})$  is automatically generated by a computer program.

We stress that AD provides a numerical value of  $\nabla_s \mathcal{L}(\mathbf{s})$  evaluated at a specific instance of  $\mathbf{s}$  instead of generating an

Evaluation Trace				Derivatives Trace			
$\lambda_{1,2}$			$= 1$	$\bar{\lambda}_{1,2}$	$= \bar{v}_1 \frac{\partial v_1}{\partial \lambda_{1,2}}$	$= \bar{v}_1^\top c_{1,2} \frac{\mathbf{t}_1}{\ \mathbf{t}_1\ }$	$= -1$
$\lambda_{2,3}$			$= 1$	$\bar{\lambda}_{2,3}$	$= \bar{v}_3 \frac{\partial v_3}{\partial \lambda_{2,3}}$	$= \bar{v}_3^\top c_{2,3} \frac{\mathbf{t}_2}{\ \mathbf{t}_2\ }$	$= -1$
$v_1$	$= \lambda_{1,2} \times c_{1,2} \frac{\mathbf{t}_1}{\ \mathbf{t}_1\ }$	$= 1 \times \frac{[1,0,0]}{1}$	$= [1, 0, 0]$	$\bar{v}_1$	$= \bar{v}_2 \frac{\partial v_2}{\partial v_1}$	$= \bar{v}_2 \times 1$	$= [-1, 0, 0]$
$v_2$	$= v_1 + \mathbf{p}_1$	$= [1, 0, 0] + [0, 0, 0]$	$= [1, 0, 0]$	$\bar{v}_2$	$= \bar{v}_4 \frac{\partial v_4}{\partial v_2}$	$= \bar{v}_4 \times 1$	$= [-1, 0, 0]$
$v_3$	$= \lambda_{2,3} \times c_{2,3} \frac{\mathbf{t}_2}{\ \mathbf{t}_2\ }$	$= 1 \times \frac{[1,0,0]}{1}$	$= [1, 0, 0]$	$\bar{v}_3$	$= \bar{v}_4 \frac{\partial v_4}{\partial v_3}$	$= \bar{v}_4 \times 1$	$= [-1, 0, 0]$
$v_4$	$= v_3 + v_2$	$= [1, 0, 0] + [1, 0, 0]$	$= [1, 0, 0]$	$\bar{v}_4$	$= \bar{v}_5 \frac{\partial v_5}{\partial v_4}$	$= \bar{v}_5 \times 1$	$= [-1, 0, 0]$
$v_5$	$= v_4 - \bar{\mathbf{p}}_3$	$= [2, 0, 0] - [3, 0, 0]$	$= [-1, 0, 0]$	$\bar{v}_5$	$= \bar{v}_6 \frac{\partial v_6}{\partial v_5}$	$= \bar{v}_6 \times 2 \times v_5$	$= [-1, 0, 0]$
$v_6$	$= v_5^\top \cdot v_5$	$= [-1, 0, 0]^\top \cdot [-1, 0, 0]$	$= 1$	$\bar{v}_6$	$= \bar{v}_7 \frac{\partial v_7}{\partial v_6}$	$= \bar{v}_7 \times 0.5 \times \sqrt{v_6}$	$= 0.5$
$v_7$	$= \sqrt{v_6}$	$= \sqrt{1}$	$= 1$	$\bar{v}_7$	$= \bar{v}_8 \frac{\partial v_8}{\partial v_7}$	$= \bar{v}_8 \times 2 \times v_7$	$= 1$
$v_8$	$= v_7 \times v_7$	$= 1 \times 1$	$= 1$	$\bar{v}_8$	$= \bar{v}_9 \frac{\partial v_9}{\partial v_8}$	$= \bar{v}_9 \times 0.5$	$= 0.5$
$v_9$	$= v_8 \times 0.5$	$= 1 \times 0.5$	$= 0.5$	$\bar{v}_9$	$= \bar{\mathcal{L}}(\mathbf{s}) \frac{\partial \mathcal{L}(\mathbf{s})}{\partial v_9}$	$= \bar{\mathcal{L}}(\mathbf{s}) \times 1$	$= 1$
$\mathcal{L}(\mathbf{s})$			$= 0.5$	$\bar{\mathcal{L}}(\mathbf{s})$			$= 1$

Table 3: Automatic differentiation (AD). To evaluate the gradient  $\nabla_{\mathbf{s}} \mathcal{L}(\mathbf{s})$  of Equation 8 in Section 3.2.1, reverse-mode AD operates on two computation traces: firstly, one evaluation trace (left-hand side) and secondly, one derivatives trace (right-hand side). To construct the former, AD evaluates Equation 8 and keeps track of all the elementary operations that modify the optimization parameters  $\mathbf{s} = [\lambda_{1,2}, \lambda_{2,3}]$  (in this case, the length of the edges  $\mathbf{e}_{1,2}$  and  $\mathbf{e}_{2,3}$ ), and the sequence in which they alter them. The output of each basic operation is stored in intermediary variables  $v_i$  which finally become interconnected nodes in the computation graph we show in Figure 4c. AD calculates partial derivatives of each of the nodes with respect to  $\mathcal{L}(\mathbf{s})$  (i.e. the *adjoints*,  $\bar{v}_i$ ) walking in reverse over the edges of the graph and applying the chain rules. The walk starts from the last operation tracked in the evaluation trace and ends when  $\mathbf{s}$  is reached. The adjoints of the optimization parameters are finally the entries in the gradient,  $\nabla_{\mathbf{s}} \mathcal{L}(\mathbf{s}) = [-1, -1]$ . After [39].

analytical expression for it. Nevertheless, the AD output is adequate for our purposes since we use the value of  $\nabla_{\mathbf{s}} \mathcal{L}(\mathbf{s})$  to minimize Equation 8, regardless of what the underlying analytical expression might be. We refer the reader to [38, 39] for a detailed theoretical treatment on how reverse-mode AD evaluates derivatives of algorithmically expressed functions. To illustrate how AD operates specifically through the weeds of the CEM framework, we supplement the discussion with a toy constrained form-finding example.

### 3.2.1. Example

Consider a two-segment compression chain subjected to an horizontal force  $\mathbf{q}_1$ . Figure 4a shows the topology diagram  $T$ , the internal force states  $\mathbf{C}$  and the design parameters  $\mathbf{x}$ . The compression-only diagram  $F$  corresponding to the state of static equilibrium  $\mathbf{u}$  output by the CEM form-finding algorithm is given in Figure 4b. In this example, we impose a geometric restriction on the position of node  $\mathbf{v}_3$ : it should land at  $\bar{\mathbf{p}}_3 = [3, 0, 0]$ . However, the resulting position  $\mathbf{p}_3 = [2, 0, 0]$  is away from the target.

We are deliberately unsure of what combination of trail edge lengths  $\lambda_{i,j}^l$  would result in a constrained state of static equilibrium  $\bar{\mathbf{u}}$  that matches  $\bar{\mathbf{p}}_3$ . To solve this constrained form-finding problem, we set the two trail edge lengths as optimization variables such that  $\mathbf{s} = [\lambda_{1,2}, \lambda_{2,3}] = [1, 1]$ . The superscript  $l$  in  $\lambda_{i,j}^l$  is dropped in this example for legibility. The only constraint function used is  $g_1$  from Table 2 and the penalty factor  $w_1$  is set to  $w_1 = 1$ .

The value of the gradient that reverse-mode AD computes is  $\nabla_{\mathbf{s}} \mathcal{L}(\mathbf{s}) = [-1, -1]$ . As expected, the negative magnitude of the partial derivatives in the gradient indicates that adjusting  $\mathbf{s}$  in the opposite direction of the  $\nabla_{\mathbf{s}} \mathcal{L}(\mathbf{s})$  would elongate both

trail edges for  $\mathbf{p}_3$  to move closer to the target position  $\bar{\mathbf{p}}_3$  after the next optimization step. Reverse-mode AD arrives at  $\nabla_{\mathbf{s}} \mathcal{L}(\mathbf{s}) = [-1, -1]$  after processing one forward and one reverse computation trace, one after the other, as we show in Table 3.

First, AD builds a forward evaluation trace (also called a Wenger list [47]) once it calculates the output value of the objective function  $\mathcal{L}(\mathbf{s})$ . During the assembly of the evaluation trace, AD keeps track of the sequence of operations that interact with the entries in  $\mathbf{s}$  in their journey towards  $\mathcal{L}(\mathbf{s})$ . The evaluation trace is broken next into a sequence of elementary mathematical operations, such as sums, divisions and multiplications, whose outputs are stored in intermediary variables  $v_i$ . Dependency relations between the variables  $v_i$  are finally represented as nodes and edges in a computation graph [48] which we show for this example in Figure 4c. In this example, from the 42 steps that Algorithm 1 comprises, only one modifies  $\mathbf{s}$  which corresponds to Equation 1. We highlight the capability of AD to identify and register this automatically despite the multiple loops and conditional statements present in Algorithm 1.

Once the evaluation trace is complete, reverse-mode AD backpropagates derivatives on the nodes of the computation graph that displayed in Figure 4c. We present the derivatives trace of our example on the right-hand side of Table 3. This reverse derivatives trace starts off at the value of the objective function  $\mathcal{L}(\mathbf{s})$  and ends once the nodes in the graph that correspond to the optimization parameters  $\mathbf{s}$  are reached. Unlike forward-mode AD, only one pass over the entire computation graph suffices to compute  $\nabla_{\mathbf{s}} \mathcal{L}(\mathbf{s})$  [49]. As AD walks in reverse over the graph, it calculates the partial derivative of  $\mathcal{L}(\mathbf{s})$  with respect to every intermediate node using the chain rule. This partial derivative  $\bar{v}_i$ , called an *adjoint*, quantifies the sensitivity



of the output  $\mathcal{L}(\mathbf{s})$  to changes in the value of an intermediary variable  $v_i$  as expressed in Equation 12.

$$\bar{v}_i = \frac{\partial \mathcal{L}(\mathbf{s})}{\partial v_i} = \sum_j \bar{v}_j \frac{\partial v_j}{\partial v_i} \quad (12)$$

The calculation of  $\bar{v}_i$  is carried out by looking at each of the  $j$  immediate children nodes of the variable  $v_i$  in the computation graph [48, 50]. In this example, the value of the gradient finally results from the adjoints of the optimization parameters  $\nabla_{\mathbf{s}} \mathcal{L}(\mathbf{s}) = [\bar{\lambda}_{1,2}, \bar{\lambda}_{2,3}]$  where their partial derivatives are scaled by the adjoints  $\bar{v}_1$  and  $\bar{v}_3$ , such that  $\bar{\lambda}_{1,2} = \bar{v}_1 \frac{\partial v_1}{\partial \lambda_{1,2}}$  and  $\bar{\lambda}_{2,3} = \bar{v}_3 \frac{\partial v_3}{\partial \lambda_{2,3}}$ .

### 3.3. Design tool

With the goal of making our work usable and reproducible, the CEM framework and the extensions presented hitherto are consolidated in a standalone, open-source design tool called `compas_cem` [51]. The tool is written in Python [52] and is integrated to the COMPAS framework, a computational ecosystem for collaboration and research in architecture, engineering, fabrication, and construction [53]. As a COMPAS extension, `compas_cem` can interface seamlessly with other packages in the COMPAS framework to perform subsequent downstream tasks on the structures generated with this tool [54–56].

A first CEM toolkit was presented in [57] as a plugin bound to the Windows version of Grasshopper [58]. In contrast, `compas_cem` runs independently from 3D modeling software, and it makes it possible to solve constrained form-finding problems on tension-compression structures readily from the command line interface of any of three major computer operating systems: Windows, MacOS and Linux. Furthermore, COMPAS provides our tool with the necessary interfaces to be invoked directly inside Blender [59], Rhino for Windows and Rhino for MacOS [60], and Grasshopper [58]. We illustrate this possibility in the numerical validation experiments we discuss in Section 4.

Currently, `compas_cem` uses the implementations of the optimization algorithms in the `NLOpt` library [61] to minimize Equation 8, and delegates the evaluation of the gradient  $\nabla_{\mathbf{s}} \mathcal{L}(\mathbf{s})$  shown in Equation 10 with AD to `autograd` [62]. This choice of dependencies is not restrictive. In the future, we envision integrating other Python optimization and automatic differentiation libraries such as `scipy` [63] and `hyperjet` [64].

The codebase of the design tool we propose follows a modular and object-oriented structure. For a granular overview of the objects and functions that it comprises, we refer the interested reader to the latest version of the `compas_cem` manual available online [51]. We offer instead a walk-through over a minimal working example of `compas_cem` written in 60 lines of Python code and discuss how it relates to the theoretical concepts developed in Sections 2 and 3. This example, shown in Figure 5, generates the compression-only chain we saw in Section 3.2.

First, the necessary `compas_cem` imports happen in lines 1–14. A `TopologyDiagram()` object, instantiated in line 19, is a child class of the `Network()` relational datastructure from COMPAS. A `Network()` is a graph that facilitates the storage

```

1 from compas_cem.diagrams import TopologyDiagram
2 from compas_cem.elements import Node
3 from compas_cem.elements import TrailEdge
4 from compas_cem.elements import DeviationEdge
5
6 from compas_cem.loads import NodeLoad
7 from compas_cem.supports import NodeSupport
8 from compas_cem.equilibrium import static_equilibrium
9
10 from compas_cem.optimization import Optimizer
11 from compas_cem.optimization import PointConstraint
12 from compas_cem.optimization import EdgeLengthParameter
13
14 from compas_cem.plotters import FormPlotter
15
16
17 # 1. Define inputs
18 # Instantiate an empty topology diagram
19 topology = TopologyDiagram()
20
21 # Add nodes
22 topology.add_node(Node(1, xyz=[0, 0, 0]))
23 topology.add_node(Node(2))
24 topology.add_node(Node(3))
25
26 # Add edges
27 topology.add_edge(TrailEdge(1, 2, length=-1.0))
28 topology.add_edge(TrailEdge(2, 3, length=-1.0))
29
30 # Indicate support node
31 topology.add_support(NodeSupport(3))
32
33 # Add load
34 topology.add_load(NodeLoad(1, q=[1.0, 0.0, 0.0]))
35
36 # Build trails automatically
37 topology.build_trails(auxiliary_trails=False)
38
39 # 2. Form-Finding
40 # Generate form diagram in static equilibrium
41 form = static_equilibrium(topology, tmax=1, eta=1e-5)
42
43 # 3. Constrained Form-Finding
44 # Instantiate an optimizer
45 optimizer = Optimizer()
46
47 # Set target position for node 3
48 constraint = PointConstraint(3, xyz=[3.0, 0.0, 0.0])
49 optimizer.add_constraint(constraint)
50
51 # Set optimization parameters
52 optimizer.add_parameter(EdgeLengthParameter(1, 2))
53 optimizer.add_parameter(EdgeLengthParameter(2, 3))
54
55 # Solve constrained form-finding problem
56 cform = optimizer.solve(topology, "LD_SLSQP", eps=1e-6)
57
58 # 4. Visualize constrained form diagram
59 plotter = FormPlotter(cform)
60 plotter.show()

```

Figure 5: Python code that models the compression chain shown in Figures 4a and 4b with `compas_cem`.

of attributes on its vertices and edges as Python dictionaries. Therefore, the inputs to the CEM form-finding algorithm, the topology diagram  $T$  and the design parameters  $\mathbf{x}$ , are stored in

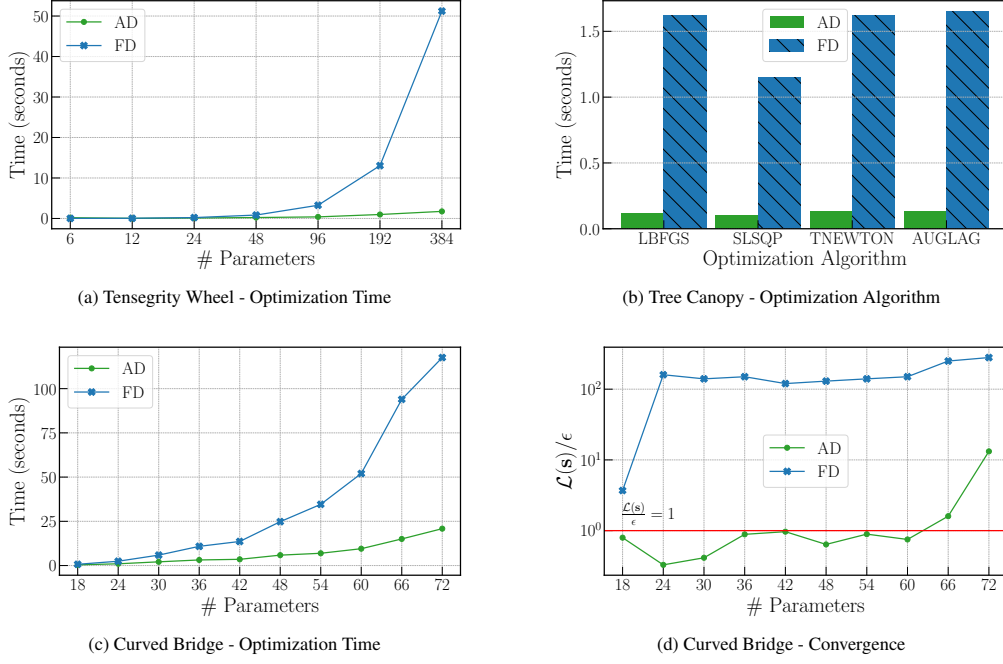


Figure 6: Performance comparison between AD and FD in our constrained form-finding experiments. The spoke wheel is optimized using the L-BFGS algorithm. The curved bridge using SLSQP. In all four figures, less is better. We show in Figures 6a and 6c that using FD with a step size  $h = 1 \times 10^{-6}$  is exponentially more expensive than AD as the number of optimization parameters is increased. Figure 6b: Disparities in the optimization time are consistent regardless of the optimization algorithm chosen. AD is at least 10 times faster per iteration than FD. Figure 6d: On average, optimization with FD does not converge and misses the convergence threshold  $\epsilon = 1 \times 10^{-6}$  by two orders of magnitude when the SLSQP algorithm is limited to run for a maximum of 100 iterations and the step size for FD is set to  $h = 1 \times 10^{-3}$ .

the same `TopologyDiagram()` object. After defining nodes, edges, supports and loads on lines 22-34, the composition of  $T$  can be formally expressed as  $\mathcal{V} = \{1, 2, 3\}$ ,  $\mathcal{E} = \{(1, 2), (2, 3)\}$ ,  $\mathcal{S} = \{3\}$ .

A graph traversal algorithm that automatically searches for trails  $\Omega$  is invoked on line 37. This algorithm takes the support node  $\mathbf{v}_3^s$  as the search starting point and moves recursively over the next trail edge  $\mathbf{e}_{i,j}$  connected until no more trail edges are found. If the boolean argument `auxiliary_trails` were set to `True`, the trail-search algorithm would attach an auxiliary trail  $\omega^a$  to any node that was not automatically assigned to a trail by the graph traversal, as exposed in Section 3.1. Only one trail is expected in this example,  $\omega_1 = \{1, 2, 3\}$ . In line 41, the CEM form-finding algorithm is invoked to output a form diagram  $F$ , conditioned on  $t_{\max} = 1$  and  $\eta_{\min} = 1 \times 10^{-5}$ . As with `TopologyDiagram()`,  $F$  is a subclass of `Network()` that self-contains the attributes that describe the generated state of static equilibrium  $\mathbf{u}$ .

The generation of a constrained form diagram  $\bar{F}$  is spread over lines 45-56. Equation 8 is minimized with the SLSQP optimization algorithm [45] from NLOpt [61] using a convergence threshold of  $\epsilon = 1 \times 10^{-6}$ . In line 48, we specify that the desired position for node  $\mathbf{v}_3$  is  $\bar{\mathbf{p}}_3 = [3, 0, 0]$ , and in lines 52-53, we define the optimization parameters  $\mathbf{s}$  as the edge lengths of both trail edges created on lines 27-28 such that  $\mathbf{s} = [\lambda_{1,2}^l, \lambda_{2,3}^l]$ . The constrained form-finding problem is solved in line 56. Internally, autograd [62] evaluates the gradient, as required by the optimization process. We plot the resulting instance of  $\bar{F}$  in line 60.

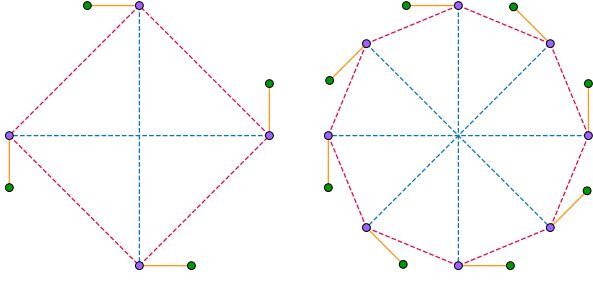
#### 4. Numerical validation

The intent of this section is to quantitatively benchmark the extensions we make to the CEM framework. We studied three structures that leverage auxiliary trails to be topologically compatible with the CEM form-finding algorithm: a self-stressed tensegrity wheel, a tree canopy and a curved suspension bridge. A graphical summary of our findings is supplied in Figure 6.

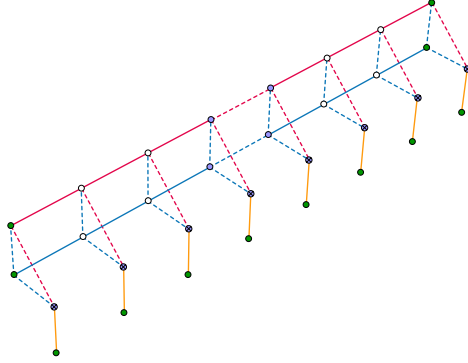
The first two structures were modeled using only deviation edges to illustrate how, in an extreme case, inserting an auxiliary trail to every node in  $T$  can relieve designers from the trail-deviation edge labeling process (see Section 2.1). The last structure follows a more conventional approach and only appends auxiliary trails at the tip of the cantilevering hangers.

In all the experiments, the structures were assumed pin-jointed and bearing only axial forces. We minimized the forces in all the auxiliary trails (except at the support nodes) by setting the target edge force  $\hat{\mu}_i$  to zero. Additional geometric constraints were imposed on the curved bridge to test the auxiliary trails extension in combination with more constraint types.

Each constrained form-finding problem was solved using automatic differentiation (AD) and finite differences (FD) as in the baseline version of the CEM framework [24]. The impact of the two differentiation schemes was compared by looking at the total optimization runtime (i.e. the elapsed time in seconds it takes an optimization algorithm to converge), the number of optimization parameters and the value of the objective function after generating a satisfactory constrained equilibrium state  $\bar{\mathbf{u}}$ .



(a) Tensegrity wheel with 4 (left) and 8 (right) sides in their perimeter.



(b) Suspension bridge with 8 hangers

Figure 7: Topology diagrams  $T$  including auxiliary trails for two of the structures studied in our experiments

Throughout our experiments, the penalty factors for all the constraints were equal and set to one,  $w = 1$ . Unless explicitly noted, the distance threshold for iterative equilibrium was fixed at  $\eta_{\min} = 1 \times 10^{-6}$ . Likewise, optimization convergence threshold was set to  $\epsilon = 1 \times 10^{-6}$ . For reference, our experiments were carried out using `compas_cem` inside Grasshopper for MacOS, on a quad-core Intel CPU clocked at 2.9 GHz.

#### 4.1. Auxiliary trails in 2D

Self-stressed structures are not subjected to external loads and are support-free. Here, a 2D self-stressed spoke wheel was modeled such that its perimeter is entirely in tension and the internal spokes in compression (Figure 8). A parametric study was carried out where we progressively increased the number of sides on the perimeter of the wheel in steps of size  $2^n$ , where  $n \in \{2, \dots, 8\}$ . Equation 8 was minimized with the L-BFGS algorithm [44].

For each configuration, the topological diagram of the wheel comprised  $2^{n+1}$  nodes and  $2^{n+1} - 0.5(2^n)$  edges, of which  $1.5(2^n)$  are deviation edges and the remainder, the edges of the auxiliary trails. The force in every deviation edge was considered an optimization parameter. While AD and FD saw similar performance when  $n < 4$ , the optimization time using FD surged exponentially as the number of parameters grew (see Figure 6a). When the number of parameters was the greatest (384), solving the constrained form-finding problem with AD

gradients took only about 3.0% of the time it took using the FD approximation.

#### 4.2. Auxiliary trails in 3D

The addition of auxiliary trails to a three-dimensional tree canopy structure was tested next (see Figure 9). We observed how the performance of AD and FD differed as the choice of optimization algorithm changed. The initial tree structure was modeled with 46 nodes and 72 deviation edges. The total number of nodes and edges in the topological diagram doubled after inserting the auxiliary trails. Unitary point loads were applied only to the nodes at the roof level of the structure.

To minimize the forces in the auxiliary trails, 186 optimization parameters were defined. These parameters consisted of the positions of the origin nodes, which were allowed to translate only in the Y and Z Cartesian directions, and the force magnitude in every deviation edge. We tested four different gradient-based optimization algorithms: L-BFGS [44], SLSQP [45], TNEWTON [46], and AUGLAG [65]. The algorithms were run for a maximum of  $t_{\max} = 200$  iterations and the step size for FD was  $h = 1 \times 10^{-6}$ .

Solving the force minimization problem was at least 10 times faster per iteration using AD irrespective of the optimization algorithm used (see Figure 6b). The optimization time with AD did not exceed 0.2 seconds/iteration whereas this value surpassed 1.0 seconds/iteration with FD. Among the four options, L-BFGS was the fastest for both differentiation schemes, requiring 76 and 120 iterations to converge for AD and FD respectively. It is worth noting that minimizing the objective

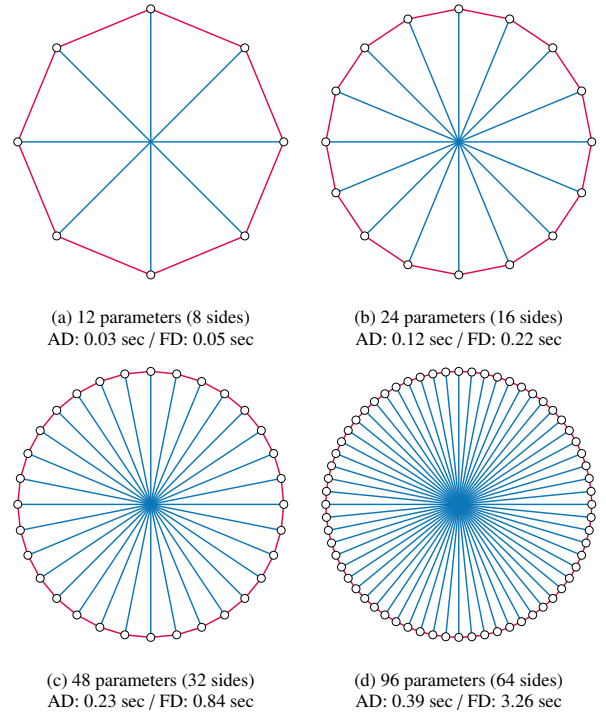


Figure 8: Constrained form diagrams  $\bar{F}$  of four self-stressed tensegrity wheels form-found using the extended CEM framework. Edges under tension and compression forces are rendered in red and blue, respectively.

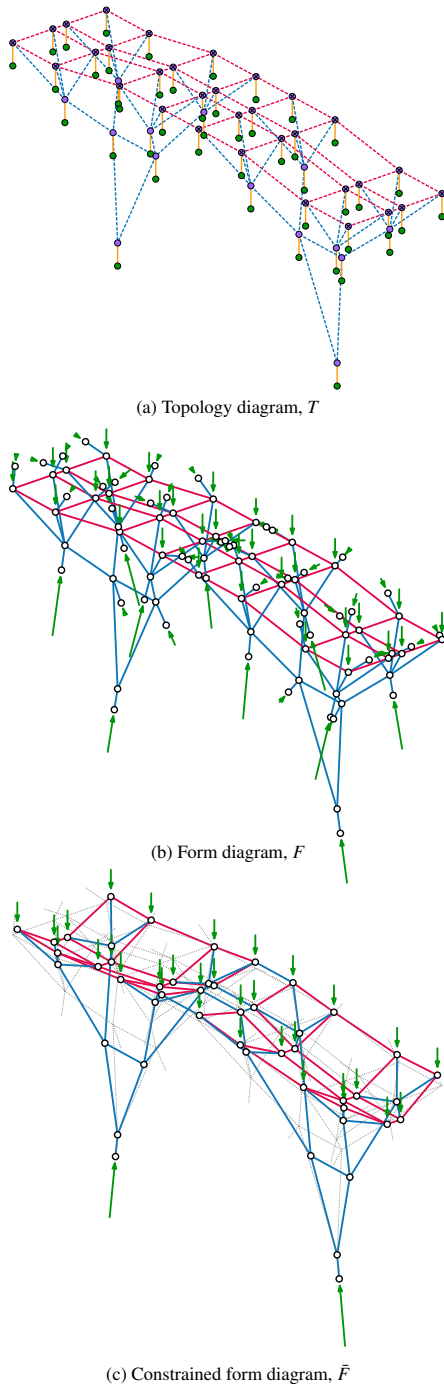


Figure 9: Tree canopy. Notice how, in the form diagram  $F$ , the auxiliary trails on the branches take a large portion of the support reaction forces. After optimizing the position of the nodes, the reaction forces in the constrained form diagram  $\bar{F}$  are taken only by the two supports at the base of the structure, while the internal forces in the auxiliary trails vanished.

function with AD was at least one order of magnitude faster in the 2D spoke wheel described in Section 3.1 than it was with the tree structure presented here. We observed a similar trend even when the size of the constrained form-finding problem was comparable and the optimization algorithm was the same: 182 parameters and a total runtime of 9.15 seconds for the tree

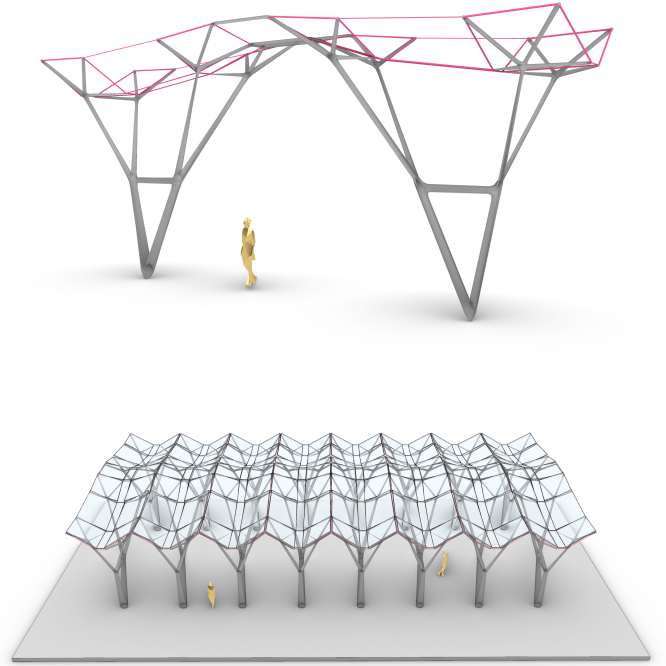


Figure 10: Architectural vision for the constrained form diagram  $\bar{F}$  shown in Figure 9. The form-found tree canopy is repeated sequentially to create a colonnade of load-bearing trees.

versus 198 parameters and a runtime of 0.98 seconds for the wheel.

A reason for this discrepancy is that, for the tree structure, both the node positions and the deviation edge forces were set as optimization parameters, whereas for the spoke wheel the optimization parameters only considered the deviation edge forces. The minimization of the auxiliary trail forces utilizing both the node positions and the internal forces of the structure is a non-linear problem that can be computationally more expensive to solve.

#### 4.3. Auxiliary trails in 3D and additional constraints

We combined force and geometric constraints to steer the form-finding of a bridge with no intermediary supports (see Figure 11). The bridge is curved in plan in the longitudinal direction and a series of triangular hangers in the transversal direction took a distributed line load produced by an eccentric runway. This torsional load was converted into unitary point loads applied to the tip of the hangers via tributary lengths. Unlike the spoke wheel and the tree structure presented in Sections 4.1 and 4.2, we modeled the topological diagram  $T$  of the bridge using a hybrid strategy: auxiliary trails were appended only to the nodes at the cantilevering end because all the other nodes in  $T$  were assigned to a standard trail on the longitudinal chords of the bridge.

The geometric constraint here was to pull the support nodes towards two predetermined vertical line rays located at either extreme of the bridge, in addition to vanishing the forces in the auxiliary trails. The rationale behind this constraint was to arrive at a form in static equilibrium subjected to a limited



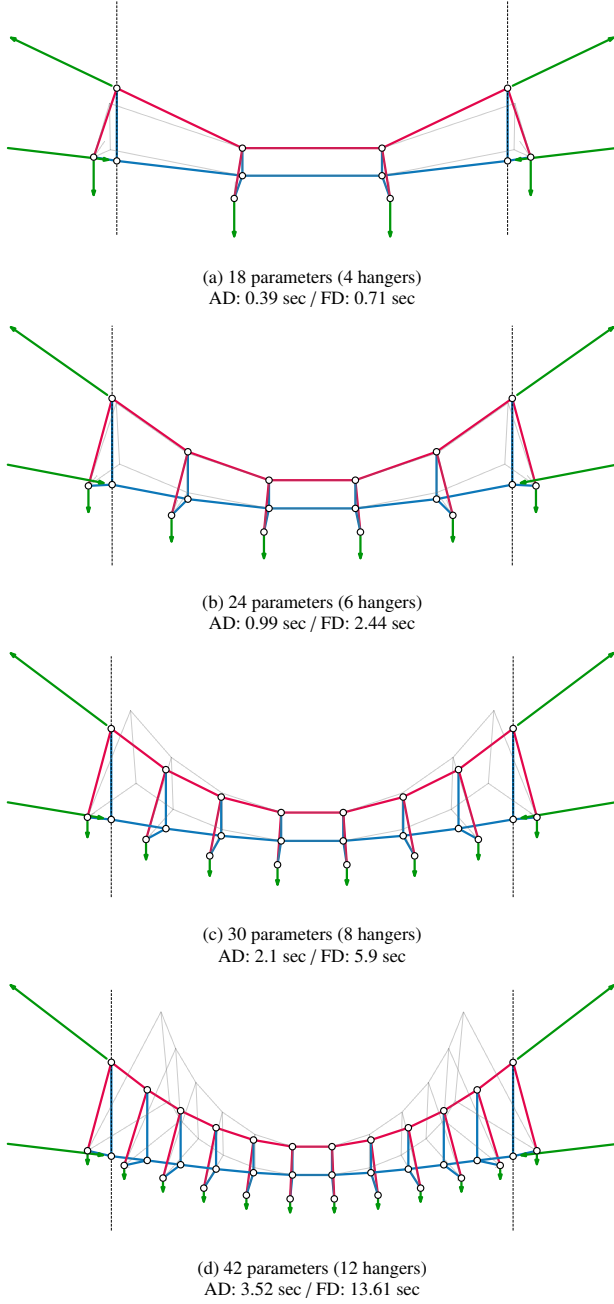


Figure 11: Sensitivity analysis for a curved suspension bridge. We show the constrained form diagrams  $\bar{F}$  for 4, 6, 8 and 12 triangular cantilevering hangers. The form diagrams  $F$  resulting from the first run of the CEM form-finding algorithm are drawn in the background with dotted lines. The forces in the auxiliary trails at the tip of the hangers have been minimized and the bridge endpoints pulled to the dashed vertical line rays in black. The solution to this constrained form-finding task is consistently faster with AD.

range of locations to anchor the bridge abutments. The forces in all the deviation edges in  $T$  were considered optimization parameters. The number of optimization parameters ranged from 18, when the number of triangular hangers was the smallest, to 72 when it was the greatest.

We compared AD and FD here with two tests. Each of the tests presented a monotonic increase in the number of

hangers, from 4 to 22, in even steps, and was solved with the SLSQP algorithm [45]. The goal of the first test was to estimate how long the constrained form-finding problem would take to converge when auxiliary trails were added only to a portion of the nodes in  $T$ . We set the step size for FD to  $h = 1 \times 10^{-6}$  but we left the total number of optimization iterations for both AD and FD unconstrained. The purpose of the second test was to find if the optimization algorithm would converge by reaching a convergence threshold of  $\epsilon = 1 \times 10^{-6}$  when the number of iterations available was restricted: we fixed a budget of 100 optimization iterations and set  $h = 1 \times 10^{-3}$  for FD.

Solving the constrained form-finding problem with AD and FD in the first test resulted in similar optimization runtimes when the number of parameters was small. However, as the number of hangers in the bridge increased, the optimization runtimes diverged exponentially (see Figure 6c). This trend concurs with the observations we made in Section 4.1. The widest gap in the optimization time was of 78.9 seconds (FD was 6.25 times slower than AD) and it occurred when the number of optimization parameters was sixty-six. In the second test, AD performed significantly better when the budget of iterations was limited. Except for the last two bridge configurations, AD met the target convergence threshold  $\epsilon$  within the preset iteration budget (see Figure 6d). In contrast, none of the optimization algorithms that used FD to calculate the gradient reached the convergence threshold  $\epsilon$ , irrespective of the number of optimization parameters, by up to two orders of magnitude.

## 5. Case study

We illustrate the potential of the extended CEM framework to support designers in practical structural design problems, especially during the conceptual design stage.

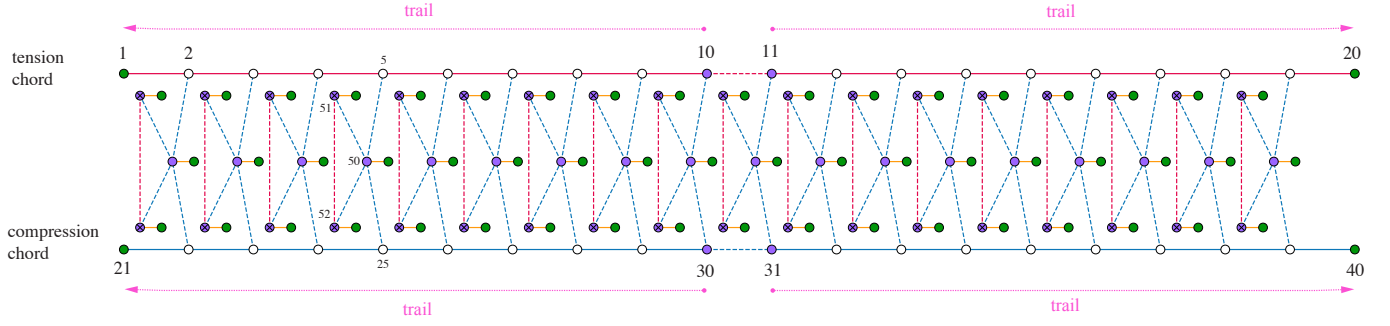
### 5.1. Design task

We designed the load-bearing structure of a spiral staircase subjected to the design constraints listed in Section 5.3. The staircase was planned to connect the ground floor to the mezzanine slab with a single run of 18 steps. The mezzanine slab was 3 meters above the ground floor and the design load was 1 kN per step. Moreover, the external perimeter of the staircase followed a semicircle with a diameter of 4 meters (Figure 12b).

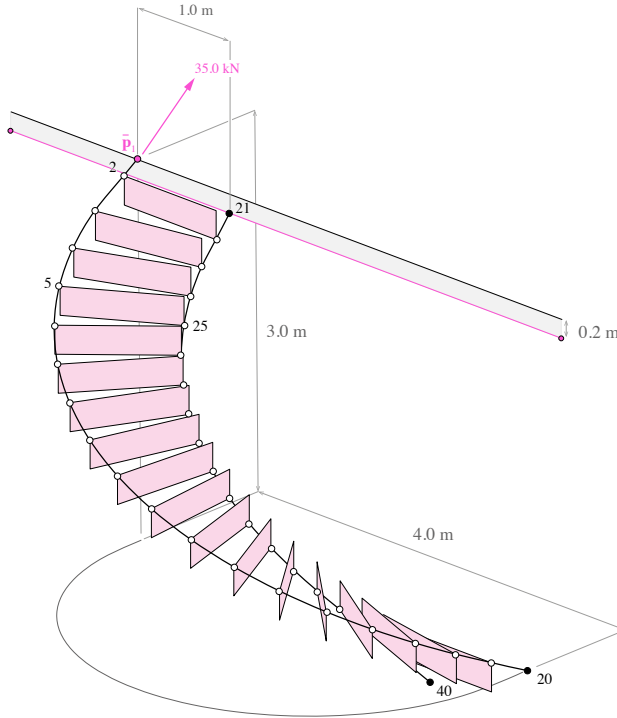
Inspired by the Fourth Bridge over the Grand Canal in Venice [66], we used the extended CEM framework to form-find a spiraling truss-like structure for the staircase. The structure was imagined to carry the applied loads via cross-shaped ribs suspended on two curving chords. The chords were initially proposed to be 1 meter apart from each other, running parallel to the run of stairs and being anchored at their intersections with the ground floor and the shallow side of the mezzanine slab.

The static equilibrium concept was to first use the tread in every step of the staircase as a tension element that tied the upper half of the compression rib underneath. Next, the goal was to resist the torsional effects produced by the forces coming from the ribs by coupling the two chords as a pair of tension-compression rings.

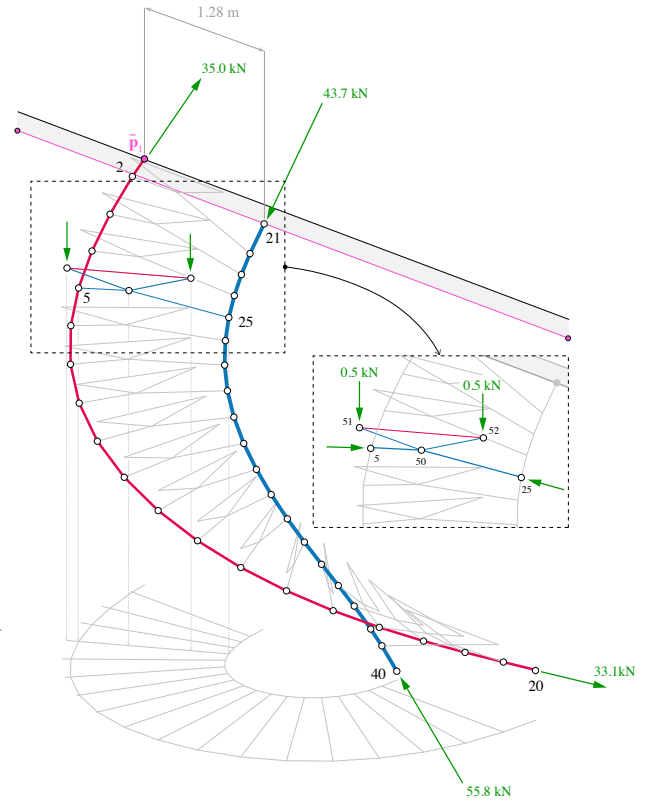




(a) Topology diagram with auxiliary trails,  $T$ . The tension and compression chords of the staircase are represented by two trails and one deviation edge each. Edges  $e_{5,50}^d, e_{25,50}^d, e_{52,50}^d, e_{52,50}^d$  model one of the 18 compression ribs and represents  $e_{51,52}^d$  its matching tension tie. The design load was of 1 kN per step was applied as  $\mathbf{q} = [0, 0, -0.5]$  kN to the end-nodes on the tension ties (e.g. to nodes  $\mathbf{v}_{51}^s, \mathbf{v}_{52}^s$ ).



(b) Design constraints



(c) Constrained form diagram,  $\bar{F}$

Figure 12: Application of the extended CEM framework to design the load-bearing structure of a spiral staircase. After constructing a topology diagram  $T$  (Figure 12a), a constrained form diagram  $\bar{F}$  (Figure 12c) that complies with a priori structural and fabrication constraints is computed using AD. The design constraints are shown in pink in Figure 12b and comprise: i) restraining the position of node  $\mathbf{v}_1^s$  to target position  $\bar{\mathbf{p}}_1 = [0, 4, 3]$ , ii) fixing the magnitude of support force  $\mathbf{r}_1$  to 35 kN, iii) constraining  $\mathbf{p}_{21}$  to lie on a continuous horizontal line 0.2 meters below  $\bar{\mathbf{p}}_1$ ; and iv) keeping the position of every pair of nodes on the chords (e.g.  $\mathbf{v}_5$  and  $\mathbf{v}_{25}$ ) on the plane defined by the funicular rib they connect to.

## 5.2. Topology diagram

The topology diagram  $T$  we used to form-find the staircase is shown in Figure 12a. We represented each of the chords with two trails connected by a single deviation edge at the middle since the chords are the two main paths for load transfer towards the supports. As secondary load-transfer elements, we modeled the 18 ribs and ties only with deviation edges and auxiliary trails.

## 5.3. Design constraints

The form-found shape of the staircase structure had to conform to a number of design requirements in addition to the minimization of the forces in the 54 auxiliary trails in  $T$ . We show these graphically in Figure 12b.

The side of the mezzanine slab where the chords were anchored had a maximum pull-out force capacity of 35 kN at position  $\bar{\mathbf{p}}_1 = [0, 4, 3]$ . As a result, the position of support node  $\mathbf{v}_1^s$  in the tension chord had to coincide with  $\bar{\mathbf{p}}_1$ , and the target



Figure 13: Architectural interpretation of the constrained form diagram  $\bar{F}$  of a spiral staircase generated with the extended CEM framework.

absolute force magnitude passing through edge  $\mathbf{e}_{1,2}$  had to be constrained to  $\bar{\mu}_{1,2} = 35 \text{ kN}$ . The position of the support node on the compression chord  $\mathbf{v}_{21}^s$  was similarly restricted to slide on a horizontal line 0.20 meters below  $\bar{\mathbf{p}}_1$ , parallel to the bottom edge of the soffit of the mezzanine slab.

Additionally, we constrained all of the nodes on the chords to the plane formed by the upper portion of the rib they connect. For example, nodes  $\mathbf{v}_5$  and  $\mathbf{v}_{25}$  in  $T$  had to lie on the plane formed by  $\mathbf{v}_{50}^o, \mathbf{v}_{51}^o, \mathbf{v}_{52}^o$ . The reasoning for this constraint was to enable the fabrication of the ribs from flat material sheets.

#### 5.4. Constrained form diagram

We parametrized this constrained form-finding problem by setting the absolute force magnitude in all the deviation edges  $\mu^d$  and the length of all the trail edges  $\lambda^t$  as entries in the vector of optimization parameters  $\mathbf{s}$ . Similarly, the position of the origin nodes on the chords  $\mathbf{v}_{10}^o, \mathbf{v}_{11}^o, \mathbf{v}_{30}^o, \mathbf{v}_{31}^o$  were allowed to translate vertically. The underlying optimization problem was minimized using the L-BFGS algorithm [44].

We show the resulting constrained form diagram  $\bar{F}$  in Figure 12c. The output values of the gradient  $\nabla_{\mathbf{s}}\mathcal{L}(\mathbf{s})$  and of the objective function  $\mathcal{L}(\mathbf{s})$  approached  $\epsilon = 1 \times 10^{-6}$ , implying that the generated  $\bar{F}$  for the staircase was satisfactory, meeting all the imposed design constraints. We can observe that some of the trade-offs made to solve this constrained form-finding

task are that the initial distance between the chord supports on the mezzanine slab increased from 1 meter to 1.28 meters and that the absolute magnitude of the reaction forces at the compression chord supports are about 25% and 60% higher than that at node  $\mathbf{v}_1^s$  post-optimization.

Figure 13 finally shows one architectural interpretation of  $\bar{F}$ .

## 6. Conclusion

In this paper, we presented, developed and validated three extensions to the CEM framework: auxiliary trails, AD and `compas_cem`. Compared to the baseline version [23, 24], our work positions the extended CEM framework as a more efficient, general and accessible approach to generate structurally efficient shapes that best meet force and geometric design constraints.

Auxiliary trails simplified the construction of valid topology diagrams for more types of structures that were difficult to be topologically modeled otherwise, such as branching structures, triangular cantilevers, and self-stressed systems. These helper trails also made it possible to explicitly model a structure only with deviation edges while still fulfilling the topological modeling rules of the CEM form-finding algorithm.

The application of AD enabled the automatic calculation of an exact gradient value of the CEM form-finding algorithm, no longer an approximation that depended on the calibration of a step size as in previous work. While the FD baseline and AD saw comparable performance for small problems, our experiments demonstrated that calculating a constrained state of static equilibrium can be exponentially faster with AD as the number of optimization parameters increases. Using AD opens up the possibility to iterate over design exploration cycles with the extended CEM framework significantly faster than before, especially for large constrained form-finding problems.

With `compas_cem`, we consolidated our work into an open-source design tool. The tool enables the formulation and the solution of constrained form-finding problems in plain and simple Python code. Furthermore, `compas_cem` enables designers to use the extended CEM framework on three different operating systems and on three distinct pieces of 3D modeling software.

The work presented herein has limitations. Computing an equilibrium state where auxiliary trails are not load-bearing hinges on the solution of a constrained form-finding problem and not on a single run of the CEM form-finding algorithm. This optimization dependency is starker when a structure is modeled entirely with deviation edges. Consequently, the risk of using auxiliary trails is to end up with an under-parametrized or an over-constrained problem where neither equilibrium nor any other design constraint is met. We also hypothesize that calculating equilibrium states for deviation-only models with the extended CEM framework has a connection to the formulation of the *Update Reference Strategy* (URS) [10] and the FDM [8, 9], and as such, form-finding deviation-only models with our approach may share their drawbacks. A deeper investigation of this relationship is left to subsequent publications.

Future work should look into hybrid modeling strategies that guide designers to best combine auxiliary trails with standard

trail and deviation edges during the construction of a topology diagram. Other future research directions are to add regularization terms to our current penalty approach to handle outlier constraints more robustly and to experiment with more types of objective functions as presented in [43]. We are also interested in leveraging more complex gradient-based optimization techniques such as Newton-based optimization methods which utilize the second-order derivatives of the system solution (i.e. the Hessian) to solve constrained form-finding problems more efficiently [36]. By delegating the computation of derivative values to a computer using AD, we can now compose arbitrary design constraints and calculate higher-order derivatives with minimal friction: the only requisites are that the constraint and the objective functions are differentiable and written in (Python) code.

The adoption of computational techniques like AD can make gradient-based optimization more accessible to researchers in the field and can propel the development of integrative and efficient frameworks that generate forms imbued with structural and non-structural design requirements. We ultimately hope our work helps to position constrained form-finding methods as viable tools to tackle practical structural design problems on a wider spectrum of structural typologies, beyond the conventional catalog of shells and cable-nets.

## 7. Acknowledgements

We thank Isabel Moreira de Oliveira from the Form-Finding Lab at Princeton University for her insightful comments during the development of this paper.

## References

- [1] W. J. Lewis, *Tension Structures: Form and Behaviour*, Thomas Telford ; Distributors, ASCE Press, London : Reston, VA, 2003.
- [2] K. Bletzinger, Fifty Years of Progress for Shell and Spatial Structures : In Celebration of the 50th Anniversary Jubilee of the IASS (1959-2009, International Association for Shell and Spatial Structures, Madrid, 2011.
- [3] J. H. Argyris, T. Angelopoulos, B. Bichat, A general method for the shape finding of lightweight tension structures, *Computer Methods in Applied Mechanics and Engineering* 3 (1) (1974) 135–149. doi:10.1016/0045-7825(74)90046-2.
- [4] B. Tabarrok, Z. Qin, Nonlinear analysis of tension structures, *Computers & Structures* 45 (5-6) (1992) 973–984. doi:10.1016/0045-7949(92)90056-6.
- [5] M. R. Barnes, Form Finding and Analysis of Tension Structures by Dynamic Relaxation, *International Journal of Space Structures* 14 (2) (1999) 89–104. doi:10.1260/0266351991494722.
- [6] A. Kilian, J. Ochsendorf, Particle-Spring Systems for Structural Form Finding, *Journal of the International Association for Shell and Spatial Structures* 46 (2) (2005) 77–84.
- [7] S. Adriaenssens, L. Ney, E. Bodarwe, C. Williams, Finding the form of an irregular meshed steel and glass shell based on construction constraints, *Journal of Architectural Engineering* 18 (3) (2012) 206–213. doi:10.1061/(asce)ae.1943-5568.0000074.
- [8] K. Linkwitz, H. J. Schek, Einige Bemerkungen zur Berechnung von vorgespannten Seilnetzkonstruktionen, *Ingenieur-Archiv* 40 (3) (1971) 145–158. doi:10.1007/BF00532146.
- [9] H.-J. Schek, The force density method for form finding and computation of general networks, *Computer Methods in Applied Mechanics and Engineering* 3 (1) (1974) 115–134. doi:10.1016/0045-7825(74)90045-0.
- [10] K.-U. Bletzinger, E. Ramm, A General Finite Element Approach to the form Finding of Tensile Structures by the Updated Reference Strategy, *International Journal of Space Structures* 14 (2) (1999) 131–145. doi:10.1260/0266351991494759.
- [11] T. Nouri Baranger, Form Finding Method of Tensile Fabric Structures: Revised Geometric Stiffness Method, *Journal of the International Association for Shell and Spatial Structures* 43 (1) (2002) 13–21.
- [12] P. Block, J. Ochsendorf, Thrust network analysis: A new methodology for three-dimensional equilibrium, *Journal of the International Association for shell and spatial structures* 48 (3) (2007) 167–173.
- [13] R. M. O. Pauletti, P. M. Pimenta, The natural force density method for the shape finding of taut structures, *Computer Methods in Applied Mechanics and Engineering* 197 (49) (2008) 4419–4428. doi:10.1016/j.cma.2008.05.017.
- [14] P. D’Acunto, J.-P. Jasienki, P. O. Ohlbrock, C. Fivet, J. Schwartz, D. Zastavni, Vector-based 3D graphic statics: A framework for the design of spatial structures based on the relation between form and forces, *International Journal of Solids and Structures* 167 (2019) 58–70. doi:10.1016/J.IJSOLSTR.2019.02.008.
- [15] M. Hablicsek, M. Akbarzadeh, Y. Guo, Algebraic 3D graphic statics: Reciprocal constructions, *Computer-Aided Design* 108 (2019) 30–41. doi:10.1016/j.cad.2018.08.003.
- [16] D. Veenendaal, P. Block, An overview and comparison of structural form finding methods for general networks, *International Journal of Solids and Structures* 49 (26) (2012) 3741–3753. doi:10.1016/j.ijsolstr.2012.08.008.
- [17] C. Fivet, D. Zastavni, A fully geometric approach for interactive constraint-based structural equilibrium design, *Computer-Aided Design* 61 (2015) 42–57. doi:10.1016/j.cad.2014.04.001.
- [18] M. Rippmann, Funicular Shell Design: Geometric approaches to form finding and fabrication of discrete funicular structures, Ph.D. thesis, ETH Zurich (2016). doi:10.3929/ETHZ-A-010656780.
- [19] G. Senatore, D. Piker, Interactive real-time physics: An intuitive approach to form-finding and structural analysis for design and education, *Computer-Aided Design* 61 (2015) 32–41. doi:10.1016/j.cad.2014.02.007.
- [20] J. Lee, T. V. Mele, P. Block, Disjointed force polyhedra, *Computer-Aided Design* 99 (2018) 11–28. doi:10.1016/j.cad.2018.02.004.
- [21] A. Nejur, M. Akbarzadeh, PolyFrame, Efficient Computation for 3D Graphic Statics, *Computer-Aided Design* 134 (2021) 103003. doi:10.1016/j.cad.2021.103003.
- [22] A. Michell, The limits of economy of material in frame-structures, *The London, Edinburgh, and Dublin Philosophical Magazine and Journal of Science* 8 (47) (1904) 589–597. doi:10.1080/14786440409463229.
- [23] P. O. Ohlbrock, J. Schwartz, Combinatorial Equilibrium Modeling, *International Journal of Space Structures* 31 (2-4) (2016) 177–189. doi:10.1177/0266351116660799.
- [24] P. O. Ohlbrock, P. D’Acunto, A Computer-Aided Approach to Equilibrium Design Based on Graphic Statics and Combinatorial Variations, *Computer-Aided Design* 121 (2020) 102802. doi:10.1016/J.CAD.2019.102802.
- [25] M. Bahr, Form Finding and Analysis of Shells And Slabs based on Equilibrium Solutions, Ph.D. thesis, ETH Zurich (2017). doi:10.3929/ETHZ-B-000182853.
- [26] D. Panozzo, P. Block, O. Sorkine-Hornung, Designing Unreinforced Masonry Models, *ACM Transactions on Graphics - SIGGRAPH* 2013 32 (4) (2013) 91:1–91:12. doi:10.1145/2461912.2461958.
- [27] H. Tamai, Advanced application of the force density method in multidisciplinary design practice by incorporating with optimization using analytical derivatives, in: J. Obrebski, R. Tarczewski (Eds.), *Proceedings of the International Association for Shell and Spatial Structures (IASS) Symposium 2013, Wroclaw, Poland, 2013*, p. 9.
- [28] J. Y. Zhang, M. Ohsaki, Adaptive force density method for form-finding problem of tensegrity structures, *International Journal of Solids and Structures* 43 (18) (2006) 5658–5673. doi:10.1016/j.ijsolstr.2005.10.011.
- [29] E. Allen, W. Zalewski, *Form and Forces: Designing Efficient, Expressive Structures*, John Wiley & Sons, 2009.
- [30] M. Miki, K. Kawaguchi, Extended Force Density Method for Form-Finding of Tension Structures, *Journal of the International Association for Shell and Spatial Structures* 51 (4) (2010) 13.

- [31] P. Malerba, M. Patelli, M. Quagliaroli, An Extended Force Density Method for the form finding of cable systems with new forms, *Structural Engineering and Mechanics* 42 (2012) 191–210. doi:10.12989/SEM.2012.42.2.191.
- [32] M. Quagliaroli, P. G. Malerba, Flexible bridge decks suspended by cable nets. A constrained form finding approach, *International Journal of Solids and Structures* 50 (14) (2013) 2340–2352. doi:10.1016/j.ijsolstr.2013.03.009.
- [33] P. O. Ohlbrock, P. D’acunto, J.-P. Jasienki, C. Fivet, Constraint-Driven Design with Combinatorial Equilibrium Modelling, in: *Proceedings of IASS Annual Symposia*, Vol. 2017, International Association for Shell and Spatial Structures (IASS), Hamburg, Germany, 2017, pp. 1–10.
- [34] K. Takahashi, L. Ney, Advanced form finding by constraint projections for structural equilibrium with design objectives, in: *Proceedings of the IASS Symposium 2018*, Boston, USA, 2018, p. 8.
- [35] P. Cuvilliers, R. Danhaive, C. Mueller, Gradient-based optimization of closest-fit funicular structures, in: K. Kawaguchi, M. Ohsaki, T. Takeuchi (Eds.), *Proceedings of the IASS Annual Symposium 2016*, Tokyo, Japan, 2016, p. 10.
- [36] J. Nocedal, S. J. Wright, *Numerical Optimization*, 2nd Edition, Springer Series in Operations Research, Springer, New York, 2006.
- [37] G. Haase, U. Langer, E. Lindner, W. Mühlhuber, Optimal Sizing Using Automatic Differentiation, in: K.-H. Hoffmann, R. H. W. Hoppe, V. Schulz (Eds.), *Fast Solution of Discretized Optimization Problems*, ISNM International Series of Numerical Mathematics, Birkhäuser, Basel, 2001, pp. 120–138. doi:10.1007/978-3-0348-8233-0\_10.
- [38] G. Corliss, C. Faure, A. Griewank, L. Hascoet, U. Naumann, *Automatic Differentiation of Algorithms: From Simulation to Optimization*, Springer, New York, NY, 2013.
- [39] A. G. Baydin, B. A. Pearlmutter, A. A. Radul, J. M. Siskind, Automatic differentiation in machine learning: A survey, *arXiv:1502.05767 [cs, stat]* (Feb. 2018). arXiv:1502.05767.
- [40] E. Unger, L. Hall, The use of automatic differentiation in an aircraft design problem, in: *5th Symposium on Multidisciplinary Analysis and Optimization*, American Institute of Aeronautics and Astronautics, Panama City Beach, FL, U.S.A., 1994, pp. 64–72. doi:10.2514/6.1994-4260.
- [41] H.-N. Cho, D.-H. Min, K.-M. Lee, H.-K. Kim, Multi-Level and Multi-Objective Optimization of Framed Structures Using Automatic Differentiation, *Proceedings of the Computational Structural Engineering Institute Conference* (2000) 177–186.
- [42] T. Oberbichler, R. Wüchner, K.-U. Bletzinger, Efficient computation of nonlinear isogeometric elements using the adjoint method and algorithmic differentiation, *Computer Methods in Applied Mechanics and Engineering* 381 (2021) 113817. doi:10.1016/j.cma.2021.113817.
- [43] P. Cuvilliers, The constrained geometry of structures: Optimization methods for inverse form-finding design, PhD Thesis, Massachusetts Institute of Technology. (2020).
- [44] J. Nocedal, Updating quasi-Newton matrices with limited storage, *Mathematics of Computation* 35 (151) (1980) 773–773. doi:10.1090/S0025-5718-1980-0572855-7.
- [45] D. Kraft, Algorithm 733: TOMP—Fortran modules for optimal control calculations, *ACM Transactions on Mathematical Software* 20 (3) (1994) 262–281. doi:10.1145/192115.192124.
- [46] R. S. Dembo, T. Steihaug, Truncated-Newton algorithms for large-scale unconstrained optimization, *Mathematical Programming* 26 (2) (1983) 190–212. doi:10.1007/BF02592055.
- [47] R. E. Wengert, A simple automatic derivative evaluation program, *Communications of the ACM* 7 (8) (1964) 463–464. doi:10.1145/355586.364791.
- [48] F. L. Bauer, Computational graphs and rounding error, *SIAM Journal on Numerical Analysis* 11 (1) (1974) 87–96.
- [49] A. Griewank, A. Walther, *Evaluating Derivatives: Principles and Techniques of Algorithmic Differentiation*, SIAM, 2008.
- [50] D. Oktay, N. McGreiv, J. Aduol, A. Beatson, R. P. Adams, Randomized Automatic Differentiation, *arXiv:2007.10412 [cs, stat]* (Jul. 2020). arXiv:2007.10412.
- [51] R. Pastrana, P. O. Ohlbrock, P. D’Acunto, S. Parascho, **COMPAS CEM: Combinatorial Equilibrium Modeling for the COMPAS framework** (2021). URL [https://arpastrana.github.io/compas\\_cem](https://arpastrana.github.io/compas_cem)
- [52] T. P. S. Foundation, **Python** (2021). URL <https://www.python.org/>
- [53] T. V. Mele, et al., **COMPAS: A framework for computational research in architecture and structures**, <http://compas.dev> (2017–2021). doi:10.5281/zenodo.2594510. URL <https://doi.org/10.5281/zenodo.2594510>
- [54] A. Liew, T. Mendez-Echenagucia, F. Ranaudo, T. Van Mele, **COMPAS FEA: Finite element analysis using Abaqus, Ansys, or OpenSEES** (2021). URL [https://https://compas.dev/compas\\_fea/](https://https://compas.dev/compas_fea/)
- [55] M. Bernhard, T. Van Mele, G. Casas, R. Clemente, N. Feihl, **COMPAS VOL: Volumetric modelling with signed distance functions** (2021). URL [https://github.com/dbt-ethz/compas\\_vol](https://github.com/dbt-ethz/compas_vol)
- [56] R. Rust, G. Casas, S. Parascho, D. Jenny, K. Dörfler, M. Helmreich, A. Gandia, Z. Ma, I. Ariza, M. Pacher, B. Lytle, Y. Huang, **COMPAS FAB: Robotic fabrication package for the compas framework**, [https://github.com/compas-dev/compas\\_fab/](https://github.com/compas-dev/compas_fab/), Gramazio Kohler Research, ETH Zürich (2018). doi:10.5281/zenodo.3469478. URL <https://doi.org/10.5281/zenodo.3469478>
- [57] P. O. Ohlbrock, P. D’Acunto, **CEM: Combinatorial Equilibrium Modeling**, release 2.00 (2021). URL <http://github.com/01e0hlbrock/CEM>
- [58] D. Rutten, **Grasshopper** (2007). URL <https://www.grasshopper3d.com/>
- [59] Blender Online Community, **Blender - free and open 3D creation software** (2021). URL <http://www.blender.org>
- [60] Robert McNeel & Associates, **Rhinoceros3d** (2007). URL <https://www.rhino3d.com/>
- [61] S. G. Johnson, The NLOpt nonlinear-optimization package (2021).
- [62] D. Maclaurin, D. Duvenaud, R. P. Adams, Autograd: Effortless gradients in numpy, in: *ICML 2015 AutoML Workshop*, Vol. 238, 2015, p. 5.
- [63] P. Virtanen, R. Gommers, T. E. Oliphant, M. Haberland, T. Reddy, D. Cournapeau, E. Burovski, P. Peterson, W. Weckesser, J. Bright, S. J. van der Walt, M. Brett, J. Wilson, K. J. Millman, N. Mayorov, A. R. J. Nelson, E. Jones, R. Kern, E. Larson, C. J. Carey, Í. Polat, Y. Feng, E. W. Moore, J. VanderPlas, D. Laxalde, J. Perktold, R. Cimrman, I. Henriksen, E. A. Quintero, C. R. Harris, A. M. Archibald, A. H. Ribeiro, F. Pedregosa, P. van Mulbregt, SciPy 1.0 Contributors, SciPy 1.0: Fundamental Algorithms for Scientific Computing in Python, *Nature Methods* 17 (2020) 261–272. doi:10.1038/s41592-019-0686-2.
- [64] T. Oberbichler, **HyperJet** (2021). doi:10.5281/zenodo.5093152. URL <https://doi.org/10.5281/zenodo.5093152>
- [65] A. R. Conn, N. I. M. Gould, P. Toint, A Globally Convergent Augmented Lagrangian Algorithm for Optimization with General Constraints and Simple Bounds, *SIAM Journal on Numerical Analysis* 28 (2) (1991) 545–572. doi:10.1137/0728030.
- [66] T. Zordan, B. Briseghella, E. Siviero, The Fourth Bridge over the Grand Canal in Venice: From Idea to Analysis and Construction, *Structural Engineering International* 20 (1) (2010) 6–12. doi:10.2749/101686610791555667.